MONTE CARLO ANALYSIS OF THE 10 MV X-RAY BEAM FROM A CLINAC-18 LINEAR ACCELERATOR

by

Corey E. Zankowski
Department of Medical Physics
McGill University, Montréal
June 1994

A Thesis submitted to the
Faculty of Graduate Studies and Research
in partial fulfillment of the requirements for the degree of
Master of Science

Name ZANKOWSKI, COREY E

Dissertation Abstracts International is arranged by broad, general subject categories. Please select the one subject which most nearly describes the content of your dissertation. Enter the corresponding four-digit code in the spaces provided.

MEDICAL PHYSICS — SUBJECT TERM

0756 — SUBJECT CODE

U·M·I

Subject Categories

THE HUMANITIES AND SOCIAL SCIENCES

COMMUNICATIONS AND THE ARTS
Architecture 0729
Art History 0377
Cinema 0900
Dance 0378
Fine Arts 0357
Information Science 0723
Journalism 0391
Library Science 0399
Mass Communications 0708
Music 0413
Speech Communication 0459
Theater 0465

EDUCATION
General 0515
Administration 0514
Adult and Continuing 0516
Agricultural 0517
Art 0273
Bilingual and Multicultural 0282
Business 0688
Community College 0275
Curriculum and Instruction 0727
Early Childhood 0518
Elementary 0524
Finance 0277
Guidance and Counseling 0519
Health 0680
Higher 0745
History of 0520
Home Economics 0278
Industrial 0521
Language and Literature 0279
Mathematics 0280
Music 0522
Philosophy of 0998
Physical 0523
Psychology 0525
Reading 0535
Religious 0527
Sciences 0714
Secondary 0533
Social Sciences 0534
Sociology of 0340
Special 0529
Teacher Training 0530
Technology 0710
Tests and Measurements 0288
Vocational 0747

LANGUAGE, LITERATURE AND LINGUISTICS
Language
- General 0679
- Ancient 0289
- Linguistics 0290
- Modern 0291

Literature
- General 0401
- Classical 0294
- Comparative 0295
- Medieval 0297
- Modern 0298
- African 0316
- American 0591
- Asian 0305
- Canadian (English) 0352
- Canadian (French) 0355
- English 0593
- Germanic 0311
- Latin American 0312
- Middle Eastern 0315
- Romance 0313
- Slavic and East European 0314

PHILOSOPHY, RELIGION AND THEOLOGY
Philosophy 0422
Religion
- General 0318
- Biblical Studies 0321
- Clergy 0319
- History of 0320
- Philosophy of 0322

Theology 0469

SOCIAL SCIENCES
American Studies 0323
Anthropology
- Archaeology 0324
- Cultural 0326
- Physical 0327

Business Administration
- General 0310
- Accounting 0272
- Banking 0770
- Management 0454
- Marketing 0338

Canadian Studies 0385
Economics
- General 0501
- Agricultural 0503
- Commerce-Business 0505
- Finance 0508
- History 0509
- Labor 0510
- Theory 0511

Folklore 0358
Geography 0366
Gerontology 0351
History
- General 0578
- Ancient 0579
- Medieval 0581
- Modern 0582
- Black 0328
- African 0331
- Asia, Australia and Oceania 0332
- Canadian 0334
- European 0335
- Latin American 0336
- Middle Eastern 0333
- United States 0337

History of Science 0585
Law 0398
Political Science
- General 0615
- International Law and Relations 0616
- Public Administration 0617

Recreation 0814
Social Work 0452
Sociology
- General 0626
- Criminology and Penology 0627
- Demography 0938
- Ethnic and Racial Studies 0631
- Individual and Family Studies 0628
- Industrial and Labor Relations 0629
- Public and Social Welfare 0630
- Social Structure and Development 0700
- Theory and Methods 0344

Transportation 0709
Urban and Regional Planning 0999
Women's Studies 0453

THE SCIENCES AND ENGINEERING

BIOLOGICAL SCIENCES
Agriculture
- General 0473
- Agronomy 0285
- Animal Culture and Nutrition 0475
- Animal Pathology 0476
- Food Science and Technology 0359
- Forestry and Wildlife 0478
- Plant Culture 0479
- Plant Pathology 0480
- Plant Physiology 0817
- Range Management 0777
- Wood Technology 0746

Biology
- General 0306
- Anatomy 0287
- Biostatistics 0308
- Botany 0309
- Cell 0379
- Ecology 0329
- Entomology 0353
- Genetics 0369
- Limnology 0793
- Microbiology 0410
- Molecular 0307
- Neuroscience 0317
- Oceanography 0416
- Physiology 0433
- Radiation 0821
- Veterinary Science 0778
- Zoology 0472

Biophysics
- General 0786
- Medical 0760

EARTH SCIENCES
Biogeochemistry 0425
Geochemistry 0996
Geodesy 0370
Geology 0372
Geophysics 0373
Hydrology 0388
Mineralogy 0411
Paleobotany 0345
Paleoecology 0426
Paleontology 0418
Paleozoology 0985
Palynology 0427
Physical Geography 0368
Physical Oceanography 0415

HEALTH AND ENVIRONMENTAL SCIENCES
Environmental Sciences 0768
Health Sciences
- General 0566
- Audiology 0300
- Chemotherapy 0992
- Dentistry 0567
- Education 0350
- Hospital Management 0769
- Human Development 0758
- Immunology 0982
- Medicine and Surgery 0564
- Mental Health 0347
- Nursing 0569
- Nutrition 0570
- Obstetrics and Gynecology 0380
- Occupational Health and Therapy 0354
- Ophthalmology 0381
- Pathology 0571
- Pharmacology 0419
- Pharmacy 0572
- Physical Therapy 0382
- Public Health 0573
- Radiology 0574
- Recreation 0575
- Speech Pathology 0460
- Toxicology 0383

Home Economics 0386

PHYSICAL SCIENCES
Pure Sciences
Chemistry
- General 0485
- Agricultural 0749
- Analytical 0486
- Biochemistry 0487
- Inorganic 0488
- Nuclear 0738
- Organic 0490
- Pharmaceutical 0491
- Physical 0494
- Polymer 0495
- Radiation 0754

Mathematics 0405
Physics
- General 0605
- Acoustics 0986
- Astronomy and Astrophysics 0606
- Atmospheric Science 0608
- Atomic 0748
- Electronics and Electricity 0607
- Elementary Particles and High Energy 0798
- Fluid and Plasma 0759
- Molecular 0609
- Nuclear 0610
- Optics 0752
- Radiation 0756
- Solid State 0611

Statistics 0463

Applied Sciences
Applied Mechanics 0346
Computer Science 0984
Engineering
- General 0537
- Aerospace 0538
- Agricultural 0539
- Automotive 0540
- Biomedical 0541
- Chemical 0542
- Civil 0543
- Electronics and Electrical 0544
- Heat and Thermodynamics 0348
- Hydraulic 0545
- Industrial 0546
- Marine 0547
- Materials Science 0794
- Mechanical 0548
- Metallurgy 0743
- Mining 0551
- Nuclear 0552
- Packaging 0549
- Petroleum 0765
- Sanitary and Municipal 0554
- System Science 0790

Geotechnology 0428
Operations Research 0796
Plastics Technology 0795
Textile Technology 0994

PSYCHOLOGY
General 0621
Behavioral 0384
Clinical 0622
Developmental 0620
Experimental 0623
Industrial 0624
Personality 0625
Physiological 0989
Psychobiology 0349
Psychometrics 0632
Social 0451

Abstract

The treatment head of the Clinac-18 medical linear accelerator was modelled using the EGS4 Monte Carlo simulation package. Photon-energy spectra for fields ranging from 2×2 cm^2 to 20×20 cm^2 in size were generated and the primary and scatter spectra were analyzed separately. The generated x-ray spectra were used in the calculation of the percent depth dose (PDD) distributions for flattened and unflattened 10 MV x-ray beams in a water phantom at a source-surface distance of 100 cm for the various field sizes. The agreement between calculated and measured depth doses is excellent.

Measurements of the dose in the build-up region show that the depth of dose maximum (d_{max}) increases with increasing field size for fields up to 5×5 cm^2 for both the flattened and unflattened beams. As the field size is increased beyond 5×5 cm^2, d_{max} decreases with increasing field size for the flattened x-ray beam while remaining nearly constant for the unflattened beam. Additionally, the surface dose of the flattened beam is found to approach that of the unflattened beam for large field sizes. Calculations show that the decrease in d_{max} as the field size is increased abc ,e 5×5 cm^2, and the rapid increase in the surface dose for the flattened x-ray beam with increasing field size, are due to the degradation of the flattened-beam parameters caused by low-energy photons produced in the flattening filter.

RÉSUMÉ

Un modèle de la tête de traitement du Clinac-18, accélérateur linéaire médical, a été developpé utilisant le programme de simulation Monte Carlo EGS4. Les spectres d'énergies de photon pour des champs de rayonnement entre 2×2 cm^2 et 20×20 cm^2 de dimension ont été générés et ces spectres ont été classifiés en deux catégories: photons-primaires et photons-diffusés. Les spectres primaires et diffusés obtenus pour chacune des dimensions du champ de rayonnement ont été analysé séparément. Les spectres de rayons X générés avec et sans filtre compensateur par le programme de simulation ont été utilisés dans les calculs de distribution de dose en profondeur dans l'eau pour une distance foyer-à-surface de 100 cm pour chaque grandeur de champ de traitement. L'accord entre les doses calculées et mesurées est excellent.

Les résultats des mesures de la dose dans la region entre la surface d'entrée et le point de dose maximale (d_{max}) montrent que la profondeur de la dose maximale augmente avec les dimensions du champ d'irradiation entre 2×2 cm^2 et 5×5 cm^2 que les faisceaux de rayons X soient compensés ou non. Une augmentation des dimensions du champ d'irradiation au-delà de 5×5 cm^2 entraîne une diminution de la profondeur de d_{max} pour les faisceaux compensés tandis que la profondeur de d_{max} pour les faisceaux non-compensés demeure practiquement inchangée. De plus, il a été établi que la dose à la surface de l'eau pour un faisceau compensé approche celui d'un faisceau non-compensé

quand le champ d'irradiation est de $20\times20\ cm^2$. Les calculs démontrent que la dégradation des faisceaux compensés, causée par des photons de basses énergies engendrés dans le filtre compensateur, explique la diminutiont de la profondeur de d_{max} et l'augmentation rapide de la dose à la surface.

ACKNOWLEDGMENTS

I am grateful for having had the opportunity to work for a man as patient and as helpful as Dr. E. B. Podgorsak. He has always allowed me to work independently, and yet was always willing to listen to my concerns and offer assistance whenever it was needed. He provided me with everything I needed to perform my work quickly and easily, no matter the expense or the time required to do so. Financial assistance was provided through Dr. Podgorsak from the Medical Research Council of Canada.

I would also like to thank the entire Medical Physics staff who have endured countless interruptions on my behalf and have always been eager to help. Many thanks are due to Dr. Fallone and Dr. Schreiner to whom I turned when I could not find Dr. Podgorsak. I express my gratitude to Joe Larkin who provided me with much information concerning the Clinac-18 and tolerated my presence at his computer terminal for several months.

I offer special thanks to my fellow students, especially William Parker, Hui Wang, and Brennan MacDonald, who were endless sources of information and who provided me with helpful criticism of my project.

Finally, I would like to thank my parents Esther and Melvin Zankowski for all of the support and love they have given me over the past few years.

TABLE OF CONTENTS

CHAPTER 2
Materials and Methods:

CHAPTER 3
Materials and Methods:

CHAPTER 4

CHAPTER 5

LIST OF FIGURES

LIST OF TABLES

CHAPTER 1
INTRODUCTION

1. INTRODUCTION

Radiation therapy, also referred to as radiation oncology, radiotherapy, or therapeutic radiology, is a clinical specialty which incorporates ionizing radiation in the treatment of malignant disease. The aim of radiotherapy is to deliver a precisely measured dose of radiation to a well-defined tumour volume with a minimal amount of damage to the surrounding healthy tissue. Although often considered a treatment modality for the palliation or prevention of the symptoms of cancer, radiotherapy is now used as a means for curing the disease by eradication of the tumour.

2. AN HISTORICAL PERSPECTIVE

A charged particle moving through a medium loses its kinetic energy through collisional and radiative losses. The latter losses result in the production of x rays and are referred to as *bremsstrahlung* meaning *braking* radiation. The radiative power of bremsstrahlung radiation is proportional to the square of the acceleration or deceleration of the charged particle.

The production of x-ray beams in low-pressure gas discharge tubes was discovered by Roentgen in 1895 [1] and almost immediately afterwards the biological effects of ionizing radiations were recognized. The first cure of cancer by radiation was reported in 1899, less than four years after Roentgen's discovery, after which time radiation therapy underwent a difficult growth period until the 1920's. In the infancy of radiotherapy, there was no dependable method for determining tissue dose, and even if there had been, the biological effects of ionizing radiation were not understood. Many physical and biological mistakes that proved to be fatal to the patient and detrimental to the radiotherapy staff were made during this growth period. Cancers completely unsuited for radiotherapy were often irradiated by physicians who had very poor understanding of the tool they were using [2]. However, many significant advances were made during this period, although the techniques were inconsistent and often irreproducible.

Initially, it was not possible to measure the output of x-ray generators, and x-ray doses were measured in terms of biological effects such as the degree of visible damage to the skin. The many adverse side-effects of radiotherapy were accepted at the time as unavoidable until the early 1920s when Coutard and Hautant presented evidence to the the *International Congress of Oncology* that advanced laryngeal cancer could be cured without treatment-induced complications [3]. After this revelation, radiotherapy was approached in a different manner and an effort was made to find optimum methods for treating cancer with radiation.

The hot-cathode x-ray tube invented by Coolidge in 1913 superseded the gas-discharge tube used by Roentgen. A cathode-ray tube produces x rays by accelerating electrons in an electric field created by a potential difference between two electrodes and then rapidly decelerating them in the anode. This technique was limited by the maximum potential difference which can be maintained between the anode and the cathode, and with it the accelerated particles attained only a relatively low energy. It was soon discovered that higher energy x-ray beams had a greater penetrability in matter, and high kilovoltage machines were sought by the medical community. Machines operating with up to 800 kV were installed in medical institutions as early as in 1932 [4].

Several different types of megavoltage x-ray generating machines were developed for medical applications. With time, the electron linear accelerator or *linac*, has proved to be the most convenient treatment machine and has become the most popular radiation source in clinical use. Medical linear accelerators are now capable of operating at several different energies and can operate as electron or photon radiation sources.

During the past 40 years, linac technology has made tremendous advances, yet a large number of basic physics problems related to the clinical radiation beams remain unsolved. The objective of this thesis is to study some of the physical properties of x-ray beams produced by medical linacs.

3. THESIS MOTIVATION AND OBJECTIVES

There are several ways in which to characterize an x-ray photon beam. In a radiotherapy clinic, one of the most essential quantities which describes the x-ray beam used for treatment of the patient is the *percent depth dose*. The percent depth dose (PDD), in particular the region surrounding the depth of maximum dose, the d_{max} region, of megavoltage x-ray beams, is a function of both the beam energy and the field size. For a given x-ray beam energy, it has been found that the depth of d_{max} below the surface of the phantom decreases with increasing field size for typical radiotherapy fields, yet for field sizes smaller than 5×5 cm^2, the position of d_{max} was observed to move further away from the surface with increasing field size. Until recently, the field size dependence of the percent depth dose was considered relatively unimportant and generally ignored in standard radiotherapy. However, it can have clinical consequences in some specialized radiotherapy techniques such as in radiosurgery (using very small field sizes) for the treatment of intracranial lesions, and in half-body and total-body irradiations (using very large field sizes) for the treatment of generalized metastatic disease and leukemia, respectively.

Some of the first studies of the field size dependence of radiotherapy beams were performed on cobalt-60 therapy units. As early as 1952, it was noticed that d_{max} could be shifted with field sizes and that if the PDD curve was normalized to the conventional d_{max} of 0.5 cm, doses in excess of 100% could be achieved in the build-up region when large field sizes were used [5]. The d_{max} shifts for cobalt-60 units have been confirmed by several other studies [6,7,8].

Observations of the field size dependence of the PDD curve were not limited only to cobalt-60 therapy machines. Several papers were published which described the change in the PDD curve with collimator opening for various linear accelerators [9,10]. It was found that for field sizes larger than 5×5 cm^2, the location of d_{max} shifted towards the surface of the phantom as the field size was increased. The only explanation for the shift in the position of d_{max} was that it was caused by scattered particles and that the amount of this contamination scatter was related to the size of the collimator opening.

In order to provide radiotherapists with the best possible dose deposition characteristics for photon beams from linear accelerators, it is necessary that medical physicists uncover the nature and the cause of the contamination inducing the changes in the percent depth dose. Some investigators suggested that the contamination was due to low energy photons [11] while most others believed that the contamination was from electrons [12,13]. At the present time, it is generally accepted that the contamination which affects primarily the dose build-up region is due to electrons.

The origin of the scattered electrons which increase the dose in the build-up region and cause the shift in d_{max} toward the surface is still under investigation. Some medical physicists believe that the contaminating electrons are produced in the collimating jaws [14] while others believe that the contaminants are produced in the flattening filter [12,13] and still others are convinced that they originate in the air between the x-ray source and the patient [15].

Determining the amount and origin of the electron contamination from these studies is complicated by the fact that not all of the studies were performed using x-ray beams of the same energy, and those that were at similar energies were often performed using linear accelerators of different makes. It is conceivable that the results found at one energy may not apply to a machine operating at a different energy. Just as importantly, individual linear accelerator design can influence the contamination profile significantly enough that conclusions based on one machine are not necessarily applicable to other machines.

In 1993, at the McGill Medical Physics Laboratory, Sixel and Podgorsak [16] studied the build-up region and the depth of maximum dose as a function of beam energy and field size for radiosurgical field sizes as well as for field sizes used in general radiotherapy. They observed that d_{max} was deepest for a field size of 5×5 cm^2 for photon beam energies in the range from 6 MV to 18 MV. Measurements of the dose in the build-up region for field sizes smaller than 10×10 cm^2 were confirmed by Monte Carlo calculations; however, at larger field sizes the calculated doses did not agree with measured data. The Monte Carlo calculations were performed using a photon energy spectrum for the Clinac-18 linear accelerator [17] with the collimating jaws open to form a 10×10 cm^2 field at the surface of the patient and did not include electron scatter.

The Monte Carlo calculations of the PDD for various field sizes performed using the photon energy spectrum for a 10×10 cm^2 field clearly could not accurately represent the physical reality of the experiment. For this reason, we extended the study, and attempted to accurately model the Clinac-18 linear accelerator treatment head and to simulate the output of the machine for the various field sizes with Monte Carlo calculations. The goal was that by including the linear accelerator head configuration in the calculations, agreement between theory and experiment, hence a detailed understanding of the PDD dependence on field size for the Clinac-18, could be achieved.

4. THESIS ORGANIZATION

A brief description of some of the methods currently available for the characterization of clinical x-ray beams is presented in the next section. The difficulties involved in the direct measurement of the x-ray spectrum and some indirect methods for describing the x-ray beam are explained. Finally, a theoretical means for calculating the x-ray spectrum from the first principles of physics is suggested.

The thesis is made up of two complementary sections: an experimental section and a theoretical Monte Carlo section. Chapter 2 provides a discussion of the apparatus necessary to complete the experimental portion of the thesis. The operation of the Clinac-18 medical linear accelerator, the x-ray source for the experimental measurements, is described in detail. Additionally, Chapter 2 describes two different means for measuring the percent depth dose and the detectors and tissue-equivalent phantoms required for each method.

In Chapter 3, the equipment used in the theoretical Monte Carlo calculations are discussed. A brief description of the EGS4 Monte Carlo computer code and the computer system used to run the EGS4 program is provided. Some of the methods used to accurately model the Clinac-18 treatment head in a time-efficient manner are discussed.

5. CHARACTERIZING THE OUTPUT OF X-RAY MACHINES

Clinical x-ray beams have a continuous photon energy spectrum extending to the kinetic energy of the electrons which generate the photons in the x-ray target. In an x-ray machine, the kinetic energy of the electrons is determined by the accelerating potential between the cathode and the anode. The first x-ray machines were described by the nominal accelerating potential; in other words, a beam of electrons accelerated by a potential difference of 100 keV would produce photons of between 0 keV and 100 keV in energy, and the corresponding x-ray beam would be referred to as a "100 kV" beam for a constant voltage machine, or a "100 kVp" beam for an alternating current machine.

Although often used, the nominal accelerating potential is not a sufficient index for the specification of radiation quality because x-ray beam properties depend on the total spectrum of photon energies comprising the beam and not only on the maximum photon energy present. Various techniques have been developed to improve the characterization of x-ray beam properties, three of which (energy spectrum, beam penetrability, and Monte Carlo calculations) are described below.

5.1. Spectral measurement.

Knowledge of the exact photon spectrum which comprises a given x-ray beam allows for a full characterization of the photon beam. However, the measurement of the x-ray spectrum produced by electrons decelerated in a target is difficult and limited by the measuring instruments. Direct measurement of the photon spectra from low output x-ray machines such as a diagnostic x-ray machine is possible with sodium iodide (NaI) scintillation spectrometers and with germanium-lithium, or Ge(Li), semiconductor spectrometers. A photon deposits its energy in these devices and an electric signal or "pulse" proportional to the energy of the photon is produced. Each pulse is sorted according to its size (energy) in a pulse-height analyzer and stored in an appropriate channel. The number of counts per channel indicates the number of photons with a given energy that are detected.

A spectrometer loses its sensitivity for a short period of time after every detection event. This period, known as *dead time*, sets a limitation on the number of events per unit time that the detector can count, hence the spectrometers are limited to a finite counting rate which cannot be exceeded [18]. In order to reduce the rate of photons reaching the spectrometer, the x-ray beam is usually passed through a pinhole and measurements must be made at a distance of 10 m from the x-ray source. Unfortunately, the small pinhole introduces scatter artifacts, and because of the 10 m separation required, corrections to the measured spectrum must be made for the attenuation in air of the photon beam.

An indirect method for determining the spectrum of an x-ray beam exists which involves the measurement of the radiation which is Compton-scattered at an angle of 90° by a foil of known material, and a subsequent reconstruction of the original spectrum by application of the Klein-Nishina formula [19]. This method obviates the counting rate problem because the amount of radiation scattered at such a large angle is approximately 10^5 times less than the amount of the primary radiation incident on the foil. However, this method introduces several uncertainties which greatly degrade the resolution. Figure 1.1 shows a sketch of several typical spectra produced by the same diagnostic x-ray tube operated at various peak kilovolt potentials measured using the Compton-scatter method. It can be seen that the maximum photon energy in each spectrum corresponds to the accelerating potential. The effect of increasing the tube potential is to increase the average energy of the x-ray beam [19].

Such spectral measurements are not possible on a linear accelerator because the x-ray fluence produced is too high. Also, the one-to-one correspondence between photon energy and output depends on the *total* absorption of the photons incident on the device rendering spectroscopic measurements of high energy photons impractical [20]. Consequently, medical physicists had to rely on measurements of beam penetrability to characterize the output from x-ray generating machines in the megavoltage range.

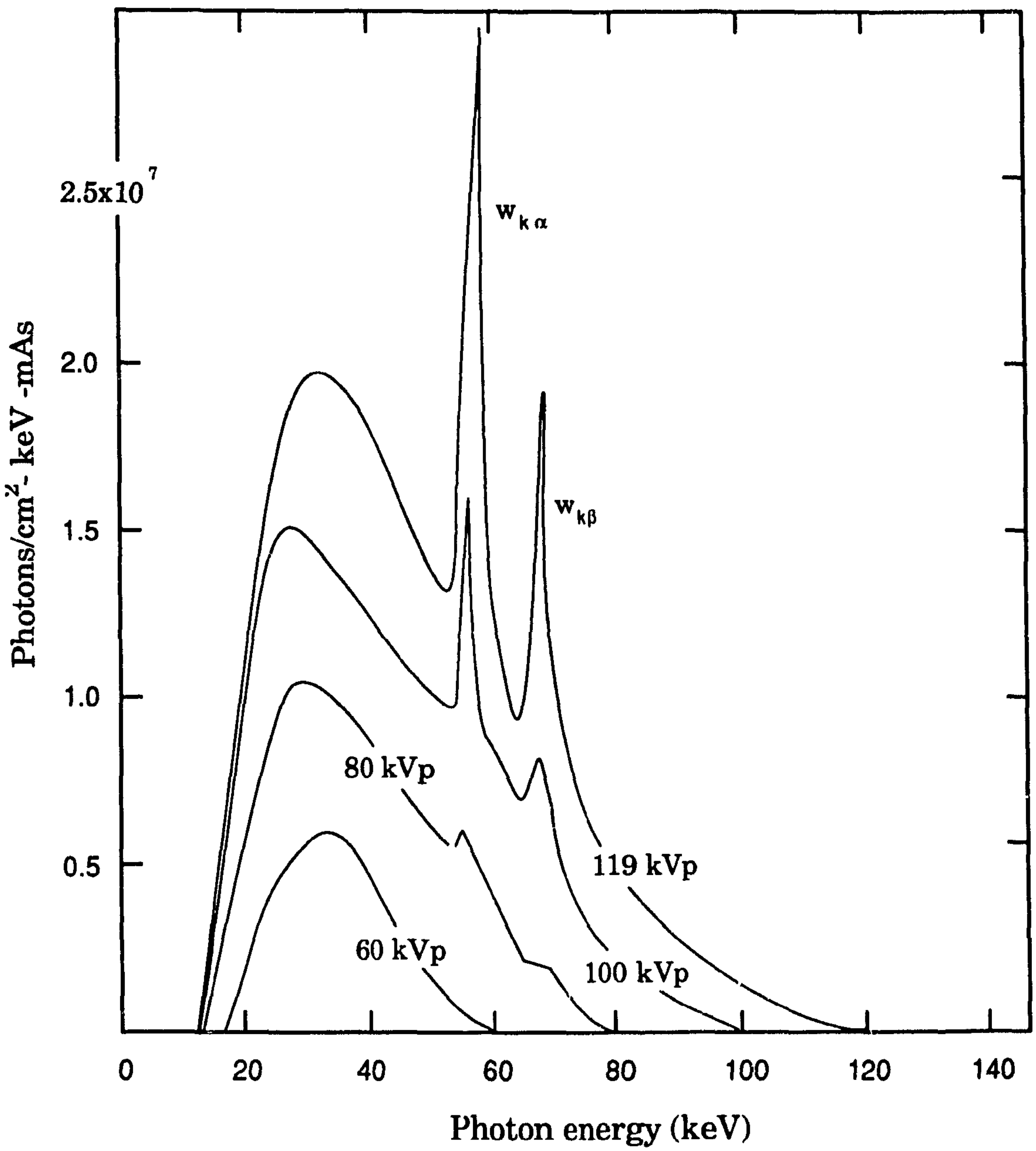

Figure 1.1 Typical photon energy spectra for a diagnostic x-ray tube operated at various peak tube potentials measured using the Compton-scatter method. The maximum photon energy corresponds to the peak kilovolt potential.

5.2. Penetrability measurements

Since in radiation therapy, one is interested in the penetrability of the radiation beam into or through the patient, it is logical to describe the nature of the radiation in terms of its ability to penetrate some material of a known composition. One way of describing the beam is through half-value layer measurements. The *half-vale layer* is defined as *the thickness of a material required to reduce the intensity of the x-ray beam to one half its original value as measured by a device calibrated to read exposure in roentgens* [20]. The number of photons in the x-ray beam is attenuated exponentially in matter. Since the attenuation coefficient is energy dependent, it is possible to calculate the *effective beam energy* from measurement of the half-value layer of an x-ray beam. The effective beam energy is defined as the energy of a *monoenergetic beam* having the same half-value layer in the medium as the polychromatic x-ray beam. The effective energy of the spectrum is useful in energy regions where the attenuation coefficient changes rapidly with energy, particularly in regions below 2 MeV. Given that the photon beam energy produced by typical linear accelerators is above 2 MeV, and that the mass-attenuation coefficient and the photon energy do not have a one-to-one correspondence in this energy region [21], the half-value layer is not a good measure for *beam quality* (beam energy) of megavoltage x-ray beams.

Another way of characterizing the x-ray beam is by measuring the central axis dose distribution with depth in a phantom. The quantity *percent depth dose* (PDD) is defined as the quotient expressed as a percentage of the absorbed dose at any depth d to the absorbed dose at a reference point d_o, along the central axis of the beam. The setup required to perform a PDD measurement is shown in Figure 1.2. For a given photon spectrum ($h\nu$), source-surface distance (SSD), and field size (A) at SSD, the percent depth dose may be expressed as

$$PDD(d, A, SSD, h\nu) = 100 \times \frac{D(d, A, SSD, h\nu)}{D(d_o, A, SSD, h\nu)} \qquad (1.1)$$,

where D is the dose at a given depth d. The reference point d_o is usually taken at the depth of maximum dose and referred to as d_{max}.

As shown in Figure 1.3, the PDD decreases with depth beyond the depth of maximum dose (d_{max}). There is an initial build-up of dose immediately beyond the phantom surface which becomes more pronounced as the energy of the beam is increased. In the case of orthovoltage machines (below 400 kV), the dose builds up to a maximum quickly and d_{max} occurs very near the surface of the phantom. For higher-energy x rays, however, d_{max} is located some distance below the surface. The region contained between the surface and d_{max} is referred to as the *dose build-up region*.

It is evident from Figure 1.3 that d_{max} increases with an increasing energy and the beam becomes more penetrating, i.e., high-energy x-ray beams deposit relatively more of their energy at a greater depth than do low-energy ones. As well, x-ray beams are more penetrating with greater SSD because the inverse-square dependence of the photon flux on depth in the phantom becomes relatively less important as the source is moved away from the surface.

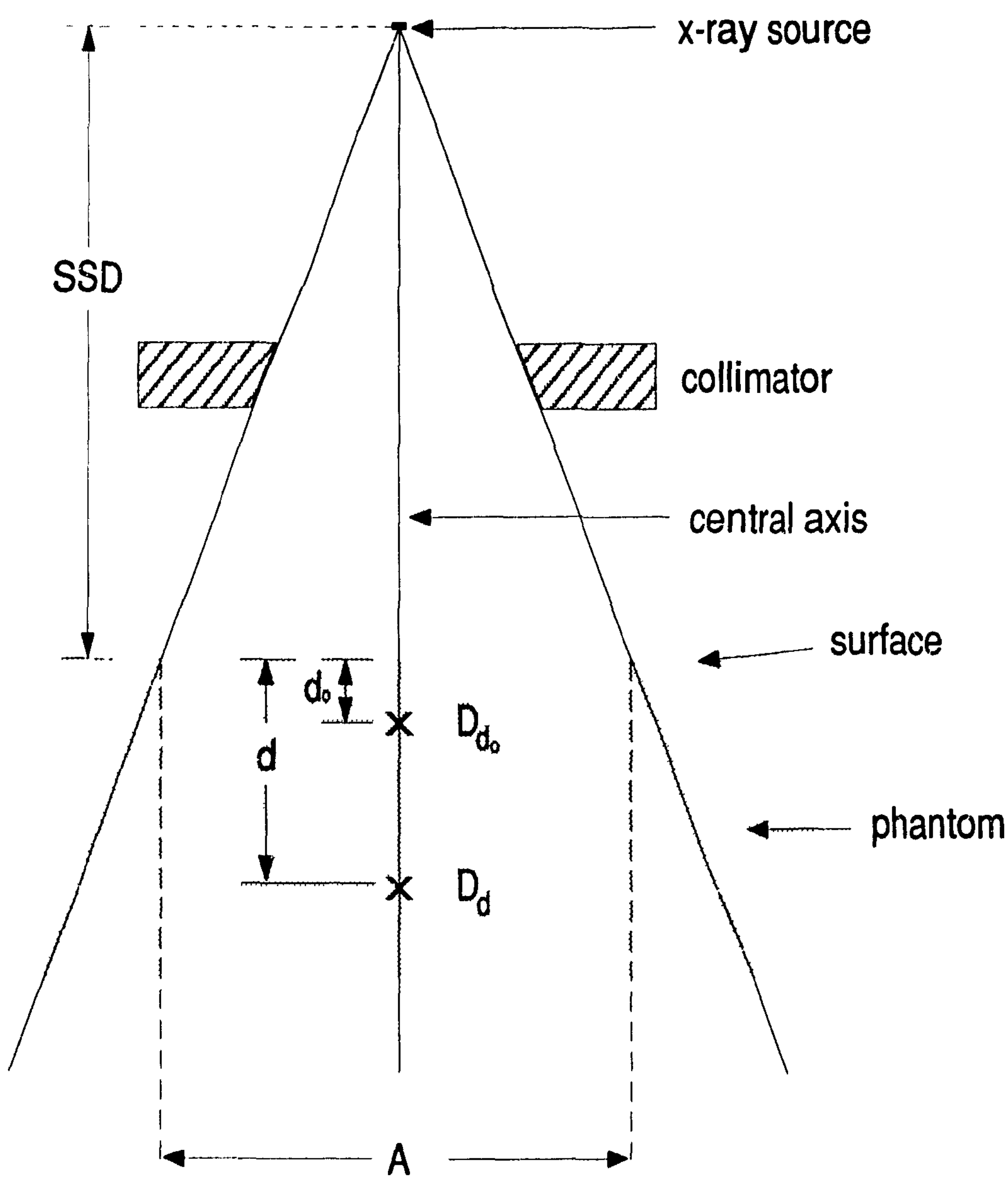

Figure 1.2 Illustration of the setup required to measure percent depth dose in a phantom. Percent depth dose is (D_d / D_{do}) x 100, where D_d is the dose at any depth d and D_{do} is the dose referenced at the depth of maximum dose, d_{max}, for a fixed source to surface distance (SSD).

Intuitively, PDD should increase with the amount of scattering material in the path of the beam, therefore, the PDD should increase with increasing field size. Since the size of the treatment beam, hence the area of scattering material, increases geometrically with depth in the phantom, the relative scatter contribution is greater with depth and more energy is deposited at larger distances from the surface. Beyond d_{max} , the dose deposited in the medium decreases because of the photon attenuation in the medium.

The physics of the build-up region is best explained in terms of the absorbed dose and a quantity known as *kerma* (kinetic energy released in the medium). The kerma is defined as the sum of initial kinetic energies of all the charged ionizing particles liberated by uncharged ionizing particles (photons)

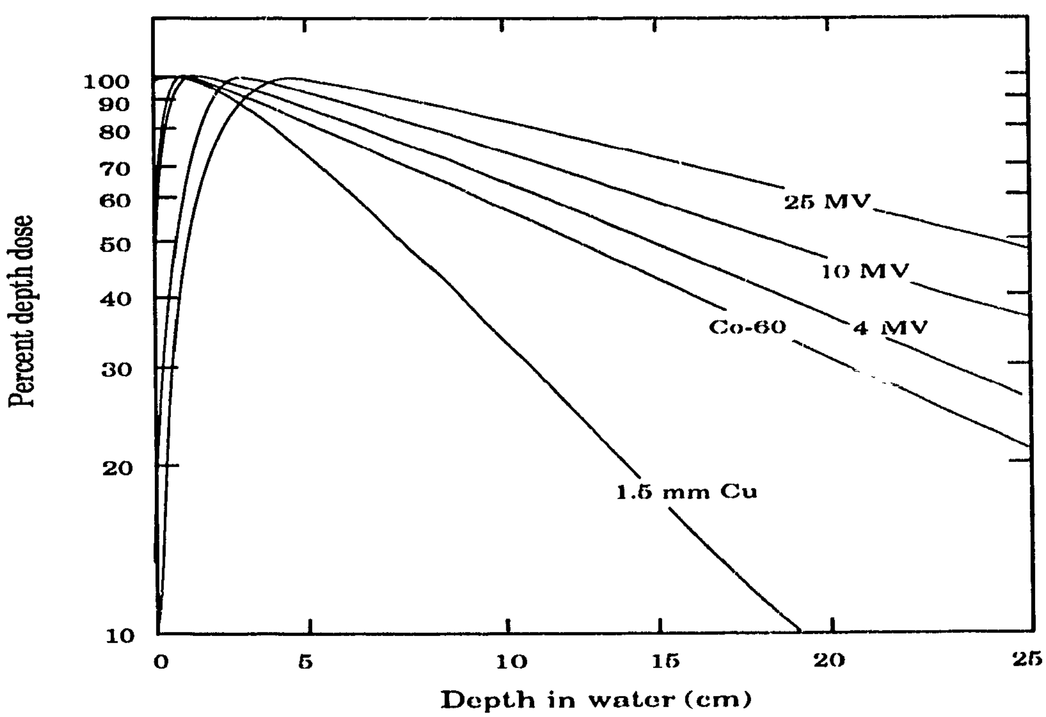

Figure 1.3 Schematic illustration of typical PDD curves in water. D_{max} occurs at greater depths with increasing energy.

per unit mass of the medium. As the high-energy photon beam enters the patient or phantom, it causes the ejection of high-energy electrons from the surface and subsequent layers of the medium. These electrons deposit their energy a significant distance away from the location of the initial interaction, thus the electron fluence and hence the dose absorbed by the medium continuously increase with depth until they reach a maximum. At the same time, the photon fluence decreases with depth, therefore the number of new electrons set into motion also decreases with depth eventually leading to a decline in the absorbed dose with depth in the medium [22].

The difference between kerma and absorbed dose is represented graphically in Figure 1.4. The relationship between the absorbed dose and kerma is

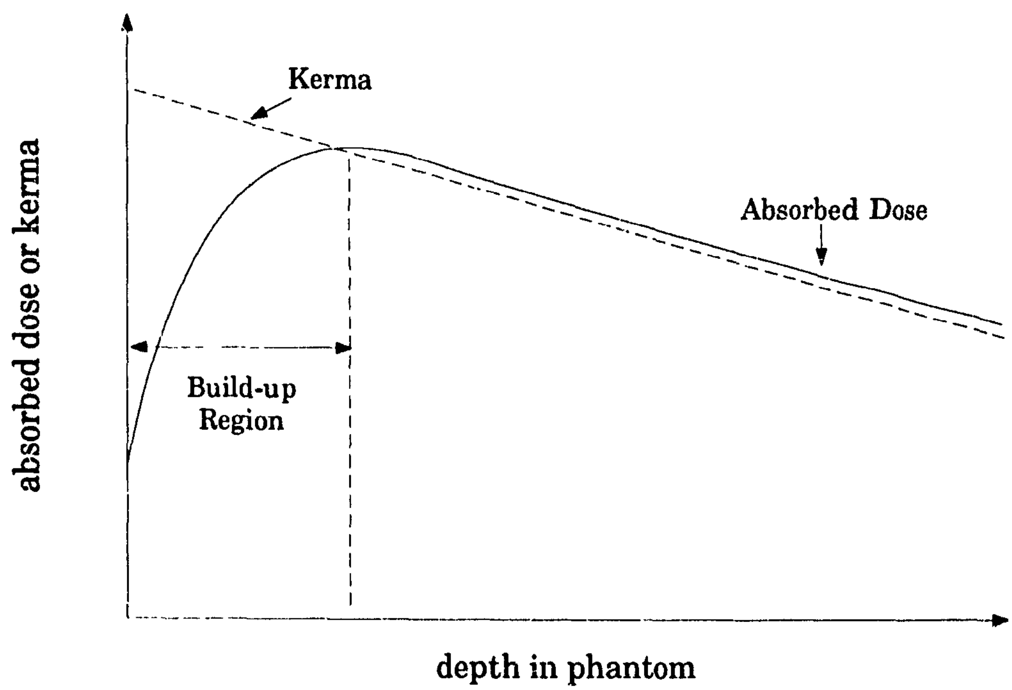

Figure 1.4 Schematic plot of absorbed dose and kerma as functions of depth in the phantom.

akin to the relationship between the activities of the daughter and parent in situations of secular equilibrium where the half-life of the daughter is much smaller than the half-life of the parent.

5.3. Monte Carlo calculations

Parameters of clinical x-ray beams generally have to be measured, however, there exists a method, based on the first principles of physics, to calculate quantities such as the percent depth dose. The method is referred to as the *Monte Carlo technique* and can be used to calculate important x-ray beam parameters. Computer programs which simulate the structure of the various sources of clinical x-ray beams can be used for this purpose. The spectra simulated in this way can then be used to calculate measurable quantities such as the half-value layer or the PDD in a medium. Agreement between calculated data and measured data would imply that the calculated data is accurate, thus the simulated particle spectrum could be considered valid.

In this manner, it is also possible to determine certain properties of the x-ray beam that could not be measured directly in the laboratory. Since the output of medical linear accelerators used in radiotherapy is too high to allow direct or indirect spectral measurements, Monte Carlo calculations are the only reliable way to determine and analyze the output spectra. The wealth of data produced by Monte Carlo techniques can readily be used to improve linear accelerator design because with Monte Carlo techniques, one can manipulate and keep track of each particle separately, therefore, the complete history of the x-ray beam is available for scrutiny.

6. REFERENCES

1. W.C. Roentgen: *On a new kind of rays* (preliminary communication). Translation of a paper read before the Physikalischemedizinische Gesellschaft of Würzburg on 28 December, 1895. Brit. J. Radiol. **4**, 32, (1931).

2. W.T. Moss, W.M. Brand, H. Battifora: Radiation Oncology, Rationale, Technique, Results, 5th edition, C.V. Mosby Company, Missouri (1979).

3. H. Coutard: *Roentgentherapy of epitheliomas of the tonsillar region, hypopharynx and larynx from 1920 to 1926*. Am. J. Roentgenol. **28**, 313, (1932).

4. C.A. Perez, L.W. Brady: Principles and Practice of Radiation Oncology, J.B. Lippincott Company, Philadelphia, Pennsylvania (1987).

5. H.E. Johns, E.R. Epp, D.V. Cormak, S.O. Fedoruk: *Depth dose data and diaphragm design for the Saskatchewan 1,000 curie cobalt unit*, Brit. J. Radiol. **25**, 302 (1952).

6. C.G. Orton, J.B. Seibert: *Surface effects of high-energy x rays at oblique incidence*, Brit. J. Radiol. **44**, 895 (1971).

7. P.S. Rao, K. Pillai, E.G. Gregg: *Effect of shadow trays on surface dose and build-up for megavoltage radiation*, Am. J. Roentgenol. **117**, 168, (1973).

8. P.M.K. Leung, M.R. Sontag, H. Maharaj, S. Chenery: *Dose measurements in the build-up region for Cobalt-60 therapy units*, Med. Phys. **3**, 169 (1976).

9. J. Aldrich, J. Andrew, H. Michaels, P. O'Brien: *Characteristics of the photon beam from a new 25-MV linear accelerator*, Med. Phys. **12**, 619 (1985).

10. G. Luxton, M.A. Astrahan: *Characteristics of the high-energy photon beam of a 25-MeV accelerator*, Med. Phys. **15**, 82 (1988).

11. J.R. Marbach, P. Almond: *Scattered photons as the cause for the observed d_{max} shift with field size in high-energy photon beams*, Med. Phys. **4**, 310 (1977).

12. J.A. Rawlinson: *High energy x -ray beams in radiotherapy*, Med. Phys. **1**, 95 (1974) (abstract).

13. P.J. Biggs, C.C. Ling: *Electrons as the cause of the observed d_{max} shift with field size in high energy photon beams*, Med. Phys. **6**, 291 (1979).

14. T.N. Padikal, J.A. Dey: *Electron contamination of a high-energy x-ray beam*, Phys. Med. Biol. **23**, 1086 (1978).

15. P.J. Biggs, M.D. Russell: *An investigation into the presence of secondary electrons in megavoltage photon beams*, Phys. Med. Biol. **9**, 1033 (1983).

16. K.E. Sixel, E.B. Podgorsak: *Buildup region and depth of dose maximum of megavoltage x-ray beams*, Med. Phys. **21**, 411 (1994).

17. R. Mohan, C. Chui: *Energy and angular distributions of photons from medical linear accelerators*, Med. Phys. **12**, 592 (1985).

18. E. Segrè: Nuclei and Particles, W.A. Benjamin, Inc., New York (1965).

19. M. Yaffe, K.W. Taylor, H.E. Johns: *Spectroscopy of diagnostic x-rays by a Compton-scatter method*, Med. Phys. **3**, 328, (1976).

20. H.E. Johns, J.R. Cunningham: The Physics of Radiology, 4th edition. Charles C. Thomas, Springfield, Illinois, U.S.A. (1983).

21. Bureau of Radiological Health and the Training Institute Environmental Control Administration: Radiological Health Handbook. U.S. Department of Health, Education, and Welfare (1970).

22. F.M. Khan: The Physics of Radiation Therapy, 2nd edition. Williams & Wilkins, Maryland, U.S.A. (1994).

CHAPTER 2
MATERIALS AND METHODS: *EXPERIMENTAL TECHNIQUES*

1. INTRODUCTION

The central-axis percent depth doses (PDD) of the Clinac-18 linear accelerator were studied for various treatment field sizes with two different techniques. The first technique employed a 3-dimensional isodose plotter with p-type semiconductor radiation detectors to provide quick beam measurements in water. The second technique, which proved more reliable but also more time consuming, was used to study the dose build-up region in more detail. This technique required a solid, tissue-equivalent phantom and an end-window parallel-plate ionization chamber for beam measurements.

Before describing the measurement techniques in detail, a discussion of the operation of the Clinac-18 is provided. Then, the tissue-equivalent phantoms used for beam measurements are described. Finally, the liquid- and solid-phantom beam characterization techniques along with a description of the radiation detectors used by each technique is given.

2. RADIATION SOURCE

A Varian Associates Clinac-18 10 MV linear accelerator located in the Radiation Oncology department of the Montreal General Hospital was used as the radiation source for the experiments described in this thesis. Since its installation in 1977, the linac has been used for conventional radiotherapy and, after some minor adaptations in 1986, its use has been extended to radiosurgery.

The main component of the Clinac-18 is a standing wave accelerator waveguide, approximately 1.4 m in length, capable of accelerating electrons to nearly the speed of light [1]. The linac has two operating modes, one of which must be selected by the operator before each treatment: the *electron mode* or the *photon mode*. In the electron mode, the linac produces electron beams ranging from 6 MeV to 18 MeV in kinetic energy while in the photon mode a fixed kinetic energy electron beam of 10 MeV is decelerated by a metal target having a thickness of approximately the electron range in the target material, to produce a 10 MV photon bremsstrahlung spectrum containing photon energies from 0 to 10 MeV.

The treatment head of the Clinac-18 is shown in Figure 2.1. It consists of an achromatic 270^{0} bending electromagnet, a retractable copper target, a primary collimating cone, a carousel holding the photon flattening filter and various electron beam scattering foils, a transmission ionization chamber, a secondary collimating system, and two sets of collimating jaws which define the radiation field with which the patient is treated. The entire head assembly is mounted on a rotating gantry having a source-axis distance (SAD) of 100 cm with the isocenter located 126 cm above the floor. Beams from two wall and one ceiling lasers converge at a point exactly 100 cm from the target and define the linac isocenter to within ± 1 mm.

The main components of the linac are illustrated schematically in Figure 2.2 along with a brief description of the generation of the radiation beam from the creation of the radiofrequency signal through the acceleration of electrons in the waveguide to the final shaping of the radiation beam in the linac head. The beam forming component of the linac may be divided into two sections: the electron accelerating section and the beam transport section. The electron accelerating section is responsible for the creation of a high energy (several MeV) electron pencil-beam, while the beam transport section transforms the pencil-beam into either a clinical photon or a clinical electron radiation beam and directs the beam toward the patient for treatment.

2.1. Electron accelerating system

The electron accelerating section of the linac is made up of two essentially separate systems: the radio frequency (RF) system and the accelerator waveguide. The RF system is connected to the accelerator waveguide by a waveguide filled with sulfur hexafluoride which passes through the rotary joint linking the linac stand to the gantry.

2.1.1. RF system. The purpose of the RF system is to provide bursts of microwave power at 2856 MHz which are used to accelerate the electrons in

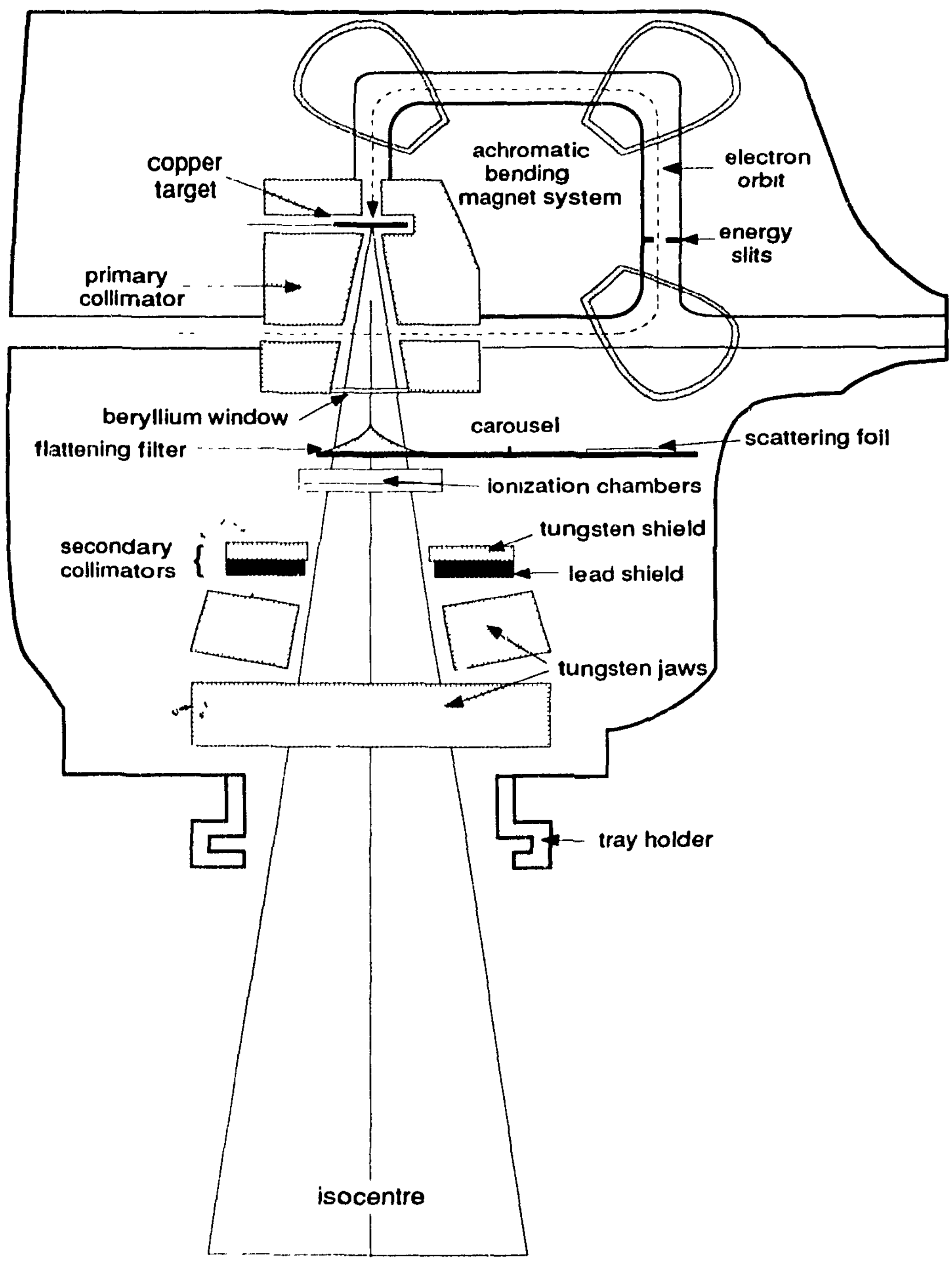

Figure 2.1 Schematic diagram of the Clinac-18 treatment head operating in the photon mode.

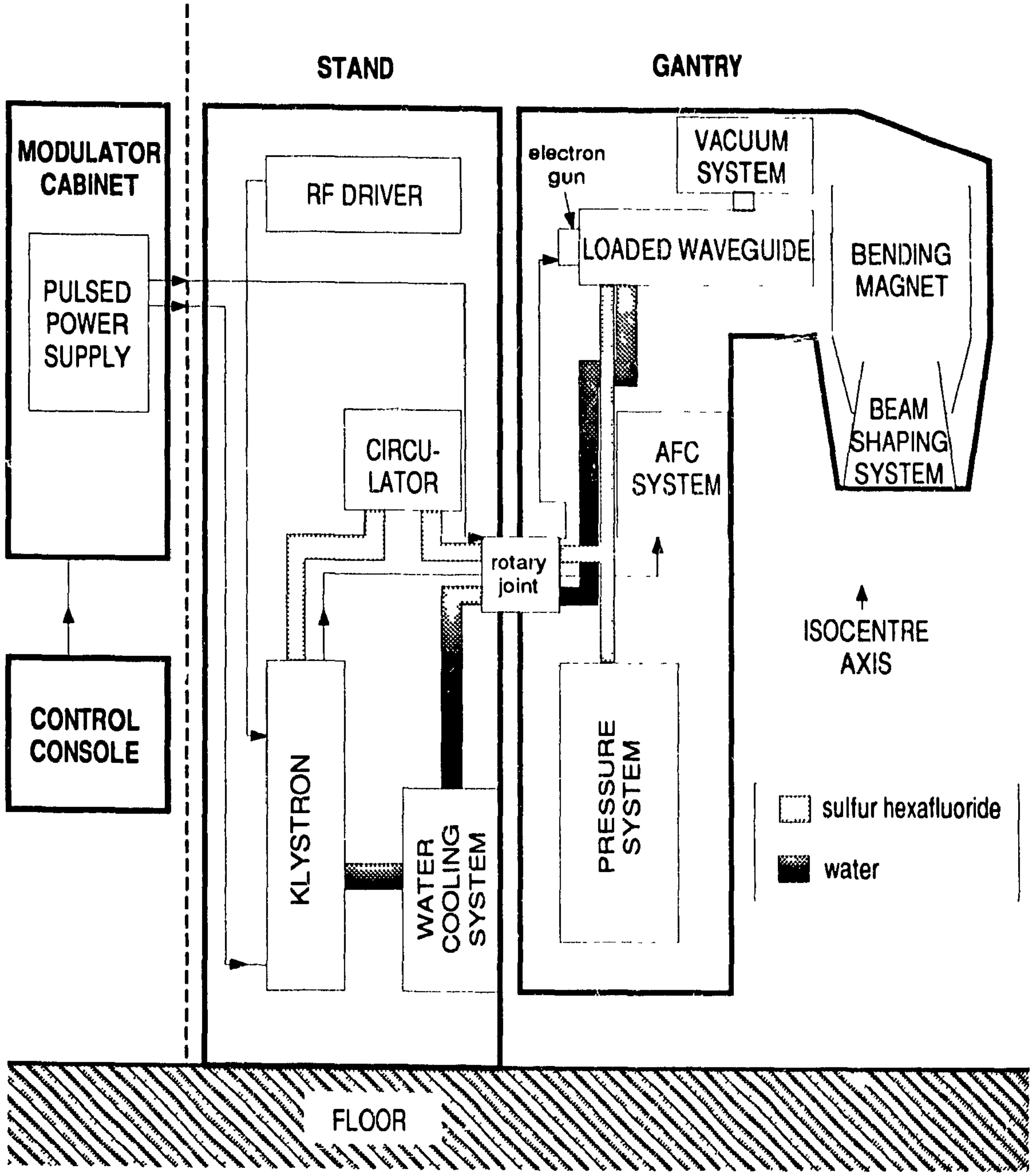

Figure 2.2 Schematic diagram of a typical isocentric linear accelerator showing the important basic components [2].

the accelerating waveguide [1]. A piezoelectric crystal located in the RF driver produces an RF signal which is then amplified to an output power level that is programmed to one of two levels depending on the modality (photon or electron) selected. A modulator pulse-modulates the 2856 MHz RF signal produced in the RF driver and sends 12 μs signal bursts through the sulphur hexafluoride-filled waveguide to an RF power amplifier which also is triggered by the modulator.

The RF power amplifier, the klystron, invented by the Varian brothers in 1937, operates in a fashion analogous to an electrical triode [3]. It is made up of two cavity resonators connected by a drift tube and is shown in Figure 2.3 [4]. The first cavity, called the "buncher" cavity, contains an electron gun and is coupled to the low-level RF signal. Electrons are emitted by the heated cathode and are accelerated toward the anode by a static potential of ~100 kV. At the same time, the RF signal excites oscillating currents in the cavity walls causing alternate sides of the buncher gap to become first positive and then negative. Thus, an electric field appears across the buncher cavity at the RF frequency that, for half a cycle, speeds up the electrons flowing through the gap; during the other half of the cycle, the electric field is in the opposite direction and slows down the electrons as they traverse the buncher. This effect is referred to as *velocity modulation.*

As the velocity-modulated electron beam passes through the drift tube, the faster electrons overtake the slower electrons to form small bunches of electrons. The length of the drift tube is chosen such that these bunches of electrons are completely formed before reaching the second cavity, the "catcher" cavity. In the catcher, the bunched electrons are rapidly decelerated in a retarding potential and radiate power at the frequency of the modulating RF signal. If the catcher cavity is of correct size, large oscillating currents will be generated within its walls. These currents induce large electric fields which oscillate at the RF frequency and are coupled to the output waveguide from the klystron. The low power microwave signal entering the klystron is thus greatly amplified: a klystron is capable of producing between 5 MW and 30 MW of peak RF power [4] and operates at an average power of 5 kW to 30 kW.

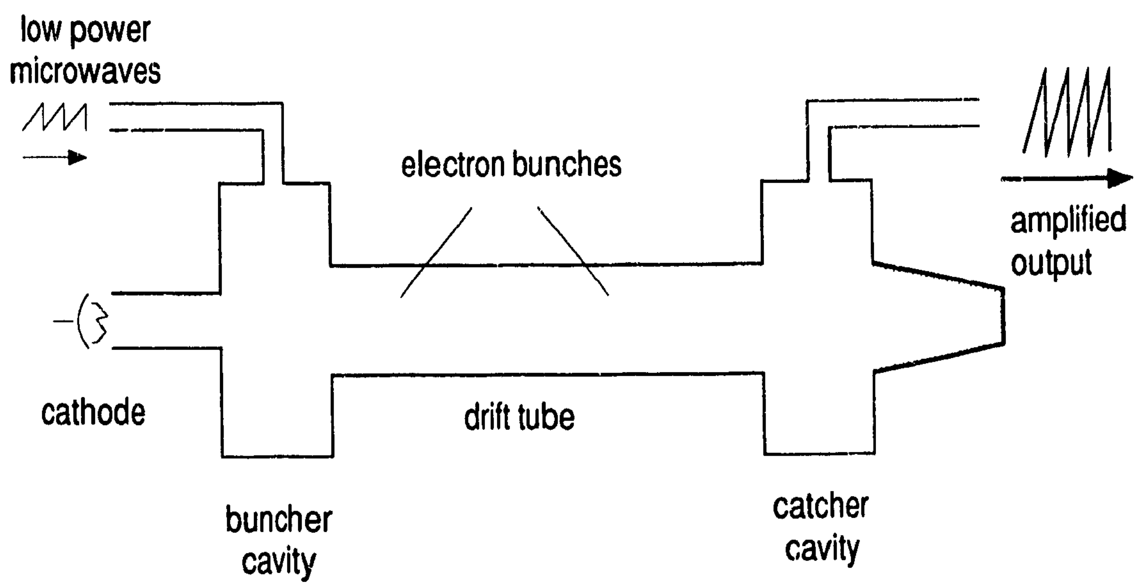

Figure 2.3 Schematic diagram of a simple two-cavity klystron RF amplifier.

The RF power signal is then passed on to the electron accelerating waveguide assembly through a circulator that serves two functions: it sets the klystron output level to that of the accelerator, and more importantly, it does not allow power reflected back from the waveguide to reach the klystron. A circulator is either a three or four port device incorporating ferrites, magnetic materials which rotate electromagnetic fields [5]. The Clinac-18 linac employs a four port circulator having the property that an RF signal incident in port 1 is coupled into port 2 only; a signal from port 2 will be coupled into port 3 only, *etc.* In this manner, the circulator redirects the power reflected from the accelerating waveguide into a high power water load to protect the klystron from damage.

2.1.2. Electron gun and standing waveguide accelerator. Most medical linacs employ a standing wave accelerating structure consisting of a series of coupled resonant cavities arranged so that at the end of travel the RF signal is reflected, giving rise to standing waves which oscillate in time. Figure 2.4 (a) [6] is a schematic representation of a waveguide with an array of equally spaced discs, $\lambda/4$ apart where λ is the wavelength of the RF signal. The arrows represent the direction of the electric fields of the forward and backward reflected wave. The shaded box denotes the location of the electron in the array after time T/4 where T is the period of the wave. In order to shorten the length of the standing wave accelerator, the zero field cavities, referred to as coupling or bimodal cavities, are normally placed aside from the main waveguide (Figure 2.4 (b)). The Clinac-18 is equipped with such a side-coupled standing waveguide which was developed by Knapp et al [7].

At one end of the accelerating waveguide is the electron gun. The electron gun is the source of electrons and injects them into the waveguide where they are bunched and accelerated in a manner similar to the klystron buncher cavity. Electrons are boiled off of the electron gun cathode and accelerated by a static electric field of between 5 keV and 25 keV, depending on the desired electron beam energy [1]. A grid located in the gun structure capable of passing or completely stopping the electron motion is used to control the injection of the electrons into the accelerating waveguide. The grid is triggered at the same time as the RF driver and the klystron modulator. The grid allows 5 μs bursts of 60 Hz - 300 Hz pulsed electrons to enter the accelerating region. The pulses are timed so that the electron bunches ride on successive peaks of the RF wave and are subject to the maximum available accelerating force of the wave.

Finally, the electron beam emerges from the resonant cavities with a kinetic energy of a discrete value between 6 MeV and 18 MeV and enters the beam transport system which carries it either toward the target (in the photon mode) or directly toward the beryllium exit window (in the electron mode). The beryllium window serves to separate the vacuum region from the surrounding environment. Beryllium is used as window material because of its low interaction cross section with both high energy photons and electrons.

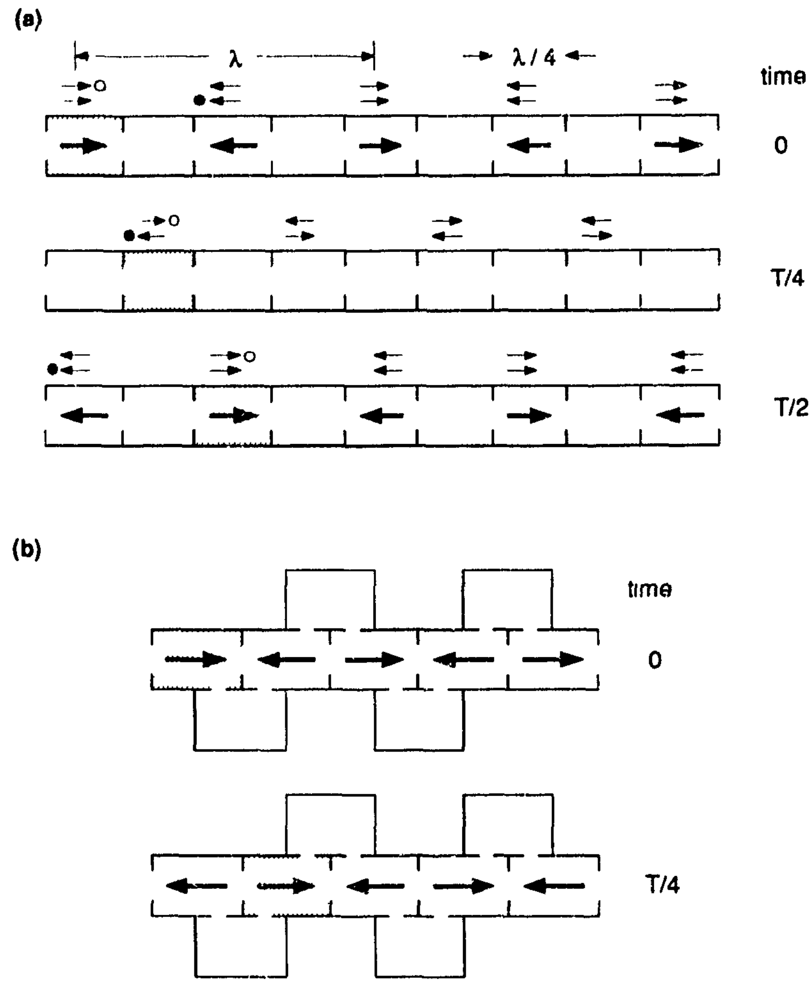

Figure 2.4 **(a)** Schematic representation of a standing waveguide with equally spaced discs, λ/4 apart. The arrows above the waveguide represent travelling waves moving in opposite directions (indicated by the black and white circles). The resulting electric fields inside the accelerating waveguide are indicated at times 0, T/4, T/2 by the large arrows. The shaded boxes represent the position of the electrons in the waveguide. **(b)** Side coupled standing waveguide where the electrons experience a positive electric field at all times.

2.2. Beam Transport Section

The beam transport section consists of two systems: the electron beam bending magnet system for controlling the beam direction and the beam conditioning system which renders the radiation beam acceptable for radiotherapy. The differentiation of the beam transport system into two sections is convenient since the treatment of the electron beam emerging from the standing waveguide is the same for both photon and electron modes, however, after the beam strikes the target (in the photon mode) or does not strike the target (in the electron mode) its treatment in the linac head is unique to the selected modality.

2.2.1. Electron beam bending magnet. After leaving the standing waveguide, the electron beam encounters an achromatic 270^0 bending magnet which changes the beam direction. The Varian Clinac-18 employs a symmetrical 270^0 three sector uniform pole gap achromatic bending magnet system proposed by Brown [5,8] and depicted in Figure 2.1. It consists of three uniform field dipole sectors connected by magnetically shielded drift tubes. The trajectories of the electrons through the system are symmetrical about the plane of symmetry which makes an angle of 135^0 with the entrance beam. This symmetry ensures that the properties of the electron beam exiting the bending magnet system are exactly the same (to second order) as the electron beam originally entering the system. A 270^0 bending magnet is used in favor of a 90^0 bending magnet because the former offers a more stable output and is achromatic. The electron beam is simultaneously focussed onto an energy analyzer slit located after the first dipole sector. The slit intercepts electrons which differ by more than ± 3% [1] from the nominal electron energy.

2.2.2. Beam conditioning system. Neither the photon beam nor the electron beam emerging through the beryllium window is suitable for radiotherapy without further conditioning. The bremsstrahlung photons produced in the target radiate in all directions and do not have a favourable energy distribution. In order to create a beam of useful dimensions with an even intensity distribution throughout the entire radiation field, the beam must be collimated and flattened. Conversely, the electron pencil-beam, which is less than 3 mm in diameter at the exit window [1], is too narrow for general use in radiotherapy. The requirements for conditioning an electron beam are different from those for a photon beam. This thesis only deals with the photon beam thus only the photon mode will be discussed.

In the *photon mode*, the 10 MeV electron beam strikes a 5 mm thick copper target and converts some of its kinetic energy into bremsstrahlung radiation. The resulting photon beam radiates energy in all directions but primarily in the forward direction, a characteristic of bremsstrahlung radiation. The 10 MeV electron beam produces a spectrum of photons ranging in energy from 0 MeV to 10 MeV with a mean photon energy of approximately 2 MeV. The spectrum produced in an x-ray target by 10 MeV electrons is referred to as a 10 MV photon spectrum.

Tungsten and lead shielding plates are used in the Clinac-18 linac to absorb those photons which cannot be used to treat the patient and would otherwise contribute to the photon contamination in the treatment room. Only a small cone of radiation is allowed to exit the linac head through the primary collimator. The primary collimator, a tungsten block with a conically shaped hole bored through its centre, defines the maximum diagonal dimension of the radiation field. It is mounted directly in front of the copper target in order to take advantage of the forward peaked bremsstrahlung radiation. The beryllium exit window is located at the end of the primary collimator opening and simply acts as the vacuum region seal.

Lying just below the exit window is a carousel containing a photon beam flattening filter and several electron beam scattering foils. In the photon mode the carousel is rotated so that the photon beam passes through the nearly conically-shaped flattening filter. The flattening filter is thickest along the central axis and therefore preferentially attenuates the photon beam along the axis. The result is a photon beam which produces a dose response curve in a tissue equivalent phantom which is uniform to within $\pm$ 3% of the central axis dose over 80% of the longitudinal and transverse axes of a 10×10 cm^2 field at an SSD of 100 cm and a depth of 10 cm [1]. The Clinac-18 located at the Montreal General Hospital is equipped with a tungsten and iron alloy flattening filter. More recent models of the Clinac-18 come with a copper flattening filter.

Beneath the carousel holding the flattening filter and the scattering foils is a dual Kapton ionization chamber for measuring the integrated dose.

The ionization chamber is divided into two independent air-filled chambers that are sealed from the external environment to minimize the effects of temperature and pressure. Kapton is used for the entrance, exit, and separation windows of the chambers as well as for the four signal plates.

The radiation beam ionizes the air in the chambers and produces a current proportional to the exposure rate. The ionization current is then integrated and converted into *dose monitor units* by a logic circuit and the integrated dose is monitored by the Clinac-18 operating console. The ionization chambers are calibrated such that, for a 10×10 cm^2 field, 100 monitor units deliver a dose of 100 cGy to the depth of maximum dose in a water phantom positioned 100 cm from the copper target. The operator sets a predetermined number of monitor units to be delivered to the patient prior to treatment, and the linac automatically terminates the x-ray production once the integrated dose read by the primary ion chamber reaches the specified level. In case of primary ion chamber malfunction, the secondary chamber will terminate treatment if its dose exceeds the stipulated primary chamber dose by 40 cGy [1]. Both ionization chambers are interrogated to test the integrity of the logic circuits before each treatment. Should the Clinac-18 shut down before delivering the required integrated dose, the operator is alerted by an audio signal and the integrated dose up to the moment of shutdown is stored on the console.

The photon flattening filter and the ionization chambers create significant amounts of scattered radiation which contribute to beam spreading. It is necessary, therefore, to redefine the photon beam. Secondary collimation of the radiation field is accomplished with a pair of obelisk-shaped secondary collimators, the upper shield being composed of tungsten and the lower shield of lead. The secondary collimators define a maximum square treatment field of $35\times35\ cm^2$.

In order to permit treatment fields smaller than 35 cm across, another collimating system is used. This adjustable collimating system is located below the secondary collimators and is the last component in the path of the photon beam before impinging on the patient. It consists of two pairs of independently movable tungsten jaws, one above the other and at right angles, which traverse arcs approximately tangential to the radiation field [1]. The tangential mounting of the collimating jaws allows for maximum field edge definition by reducing the geometrical beam penumbra. Each pair of tungsten jaws is coupled to permit rectangular fields centered on the beam axis ranging in length from 0 cm to 35 cm in both the X and Y directions.

The jaw system contains a range finder which indicates the source (target) to surface distance (SSD) from 80 to 130 cm. It also holds a field defining light designed to coincide with the actual radiation field to within ± 2 mm of the 50% isodensity line on an x-ray film at an SSD of 100 cm. The field defining light is reflected through the jaws by a mirror which is automatically removed before the beam is switched on. These two devices enable the technologists to correctly position the patient in the radiation field for the radiotherapy treatment.

3. PHANTOM MATERIALS

Typically, dose distribution data are measured in a water phantom since water closely approximates the radiation scattering and absorption properties of soft tissue (the human body is composed of approximately 75% water by weight). Additionally, water is readily available at any radiotherapy clinic and has globally reproducible radiation properties, thus water has become the radiation phantom standard. The AAPM protocol recommends that linac calibration data be expressed in terms of the absorbed dose in water [9]. Since most ionization chambers experience severe leakage effects when damp, they must be made waterproof. To circumvent this problem, solid dry phantoms have been developed.

Ideally, for a given material to serve as phantom material, it must be water or tissue equivalent, i.e., it must have the same mass density, electron density, and effective atomic number as water. Since Compton scattering is the most important interaction with tissue for megavoltage photon beams, the condition of equivalent electron density between the phantom material and water must be met.

The electron density (ρ_{el}) of a material may be calculated by using the following equation:

$$\rho_{el} = \rho_{mass} \bullet N_a \bullet \frac{Z}{A} \qquad (4.1) \quad ,$$

where

$$\frac{Z}{A} = \sum_i a_i \bullet \left(\frac{Z_i}{A_i}\right) \qquad (4.2) \quad ,$$

and ρ_{mass} is the mass density of the material, N_a is Avogadro's number

(6.023×10^{23} atoms / g atom) and a_i is the fraction by weight of the ith element of atomic number Z_i and atomic weight A_i. Mayneord [10] has defined the effective atomic number for low energies of any material in an analogous manner to Equation 4.2:

$$\bar{Z} = \left(\sum_i a_i Z_i^{2.94}\right)^{1/2.94} \qquad (4.3)$$

This equation takes into account the roughly cubic dependence of the photoelectric effect mass-attenuation coefficient on atomic number.

4. DOSIMETRIC SYSTEMS

4.1. 3-dimensional radiation field analyzer measurements

The primary portion of the beam data acquisition was performed using a radiation field analyzer (RFA) (RFA-7, Therados, Uppsala, Sweden) which can be used as a three dimensional isodose plotter or as a two dimensional radiographic film densitometer. The three dimensional isodose plotter consists of a water-filled acrylic tank with dimensions of $63\times60\times61$ cm^3 and a set of p-type semiconductor detectors (Scanditronix, GR-p EC silicon photon field detector), one of which can be positioned by remote-control anywhere within a $50\times50\times50$ cm^3 scanning volume inside the water tank while the other is used as a stationary reference detector. Since the output of a typical linac varies on a short time scale, it is the relative signal between the two detectors that is of interest to the medical physicist.

The semiconductor detector pair is connected in the photovoltaic mode to a high quality electrometer which digitizes the signal. The position of the remotely controlled detector and the relative signal strength are recorded by the control unit, an 80186, 16-bit processor. The beam data is stored as text on the computer hard disk and can be manipulated by any computer program to calculate the required beam parameters.

The detectors used for *in-water* dose measurements in the experiments outlined in this thesis were water-proofed (encapsulated), energy-compensated, p-type silicon semiconductors designed specifically for use with photon beams [11,12]. The detectors are backed by a tungsten and epoxy mixture which captures low energy photons thereby improving the energy response of the detectors. The density of the mixture is optimized to give accurate depth dose measurements over a wide range of photon energies [13]. However, the energy compensation gives rise to directional dependence related to the radiation quality, thus it is extremely important that the detectors be correctly aligned for each measurement.

Each semiconductor detector has a well-defined sensitive volume of between 0.2 mm^3 and 0.3 mm^3 located at a water equivalent distance of 0.55 ± 0.2 mm from the front of the detector surface. Although the detector volume is small, the GR-p EC silicon detector has a signal to detector volume which is 18000 times greater than a typical ionization chamber, thus noise from the stem of the detector and the connecting cable is negligible [13]. The manufacturer of the semiconductor detectors claims that the encapsulation permits dose measurements very close to the phantom surface and that the detector can be used for the determination of dose distributions not only at depths beyond the depth of maximum dose but also in the dose build-up region. In order to verify this claim, measurements in the dose build-up region obtained with this detector were compared to results obtained with a solid phantom and an air ionization detector.

4.2. Polystyrene and air ionization chamber measurements

The absorbed dose in the build-up region was remeasured in a polystyrene phantom and an end-window parallel plate ionization chamber. Polystyrene has an electron density of 3.24×10^{23} electrons/g compared with water having 3.34×10^{23} electrons/g, and a mass density of 1.03 g/cm^3 [14] and therefore can be thought of as water equivalent. While maintaining the SSD at 100 cm, thin sheets of polystyrene ranging in thickness from 0.6 mm to 3.2 mm were piled on top of the ionization chamber to measure the absorbed dose at various depths in the phantom. To ensure that x-ray backscattering effects were correctly accounted for, at least 30 cm depth of phantom material was used for each measurement. Moreover, the lateral dimensions of the polystyrene sheets measured 30 cm across to ensure that lateral electronic equilibrium was attained for all depths. All beam measurements were performed with the output of the linac set at 30 MU so that a relative percent depth dose measurement could be made.

The Farmer end-window cylindrical parallel plate ionization chamber used for measurements in the dose build-up region has an electrode separation of 1.0 mm, a sensitive diameter of 3 mm and a diameter including the guard ring of 5.2 mm. The guard ring has two roles: it provides the ionization chamber with a constant electric field strength throughout the sensitive volume of the detector and it ensures that the electrometer measures no chamber leakage currents. The chamber has a polyethylene wall of only 2.5 mg/cm^2 thickness. In order to collect the ions produced in the air contained in the sensitive volume of the ionization chamber, a potential difference is applied across the sensitive volume. The chamber was operated at electrode polarizing potentials of -300 V and +300 V, and the average of the two measurements was taken. The amount of charge collected by the chamber electrodes was read with a Keithley Instruments 616 digital electrometer (Keithley Inc., Cleveland, Ohio).

Because of detector size limitations, the smallest field size investigated was 2×2 cm^2. Percent depth dose measurements of the Clinac-18 were performed with field sizes of 2×2 cm^2, 3×3 cm^2, 5×5 cm^2, 10×10 cm^2, 15×15 cm^2, and 20×20 cm^2. Measurements were performed both with and without the presence of the flattening filter to investigate the influence of the flattening filter on the percent depth dose.

5. REFERENCES

1. Clinac-18 maintenance manual, volume 1, Varian Associates, Palo Alto, California (1975).
2. C.J. Karzmark, R.J. Morton: A primer on theory and operation of linear accelerators in radiation therapy, U.S. Department of Health and Human Services, Food and Drug Administration, Bureau of Radiological Health, Maryland (1981).
3. R.H. Varian, S.F. Varian: *A high frequency oscillator and amplifier,* Journal of Applied Physics **10**, 321 (1939).
4. S.C. Klevenhagen: Physics of Electron Beam Therapy, Medical Physics Handbook 13, Adam Hilger Ltd, England (1985).
5. C.J. Karzmark, C.S. Nunan, E. Tanabe: Medical Electron Accelerators, McGraw-Hill, Inc (1983).
6. H.E. Johns, J.R. Cunningham: The Physics of Radiology, 4th edition, Charles C. Thomas, Springfield, Illinois (1983).
7. E.A. Knapp, B.C. Knapp, J.M. Potter: *Standing wave high energy linear accelerator structures*, Rev. Sci. Instr. **39**, 979 (1968).
8. K.L. Brown, W.G. Turnbull: *Achromatic magnetic beam deflection system,*U.S. Patent 3 876 635, issued 1975.
9. American Association of Physicists in Medicine, RTC Task Group 21: *A protocol for the determination of absorbed dose from high energy photon and electron beams,* Med. Phys. **10**, 741 (1983).

10. W.V. Mayneord: *The significance of the Röntgen,* Acta Int. Union Against Cancer **2**, 271 (1937).

11. G. Rikner: *Characteristics of a selectively shielded p-si detector in ^{60}Co and 8 and 16 MV Roentgen radiation,* Acta. Radiol. Oncol. **24**, 205 (1985).

12. G. Rikner, E. Grussel: *Selective shielding of a p-si detector for quality independence.* Acta. Radiol. Oncol. **24**, 65 (1985).

13. Scanditronix customer documentation: *The energy compensated (filtered) GR-p EC detector for water phantom measurements in photon fields.* Frank Barker Associates Inc., New Jersey.

14. F.M. Khan: The Physics of Radiation Therapy, 2nd edition. Williams & Wilkins, Maryland, U.S.A. (1994).

CHAPTER 3
MATERIALS AND METHODS:
THEORETICAL CALCULATIONS

1. INTRODUCTION

A theoretical Monte Carlo calculation of the percent depth dose (PDD) along the central axis of the beam was performed by writing a series of computer programs incorporating the EGS4 Monte Carlo simulation code and integrating them together. The first stage in the simulation process involved the accurate modelling of the Clinac-18 treatment head for various field sizes. Then a program was written which analyzed the data generated by the treatment head simulation and processed the data for use with the EGS4-supplied DOSRZ dose scoring program.

All of the simulations were performed on a Sun SPARC 10 computer station with the SunOS 4.1.3 operating system. The EGS4 programs were written in the MORTRAN3 computer language which was converted into FORTRAN77 by a MORTRAN3 FORTRAN pre-compiler. The FORTRAN code was then compiled and run using Sun FORTRAN version 1.4.

2. MONTE CARLO CALCULATIONS

Monte Carlo calculations (named after the famous city of chance) are calculations which are used to describe situations that are probabilistic in nature. Essential to all Monte Carlo calculations is the detailed knowledge of the probability distributions governing the problem at hand. First, a mathematical model based on these probability distributions is formed, and then the initial conditions describing the system are defined. By using computer generated pseudo-random numbers, the model is interrogated and, according to the response of the model, a new state is achieved. The system is allowed to evolve in this manner until one of a set of final conditions is met, at which stage the progress is terminated. The random sampling of these known probability distributions is used to determine each consecutive stage in the evolution of the system and preserves the stochastic nature of the process. The entire set of events carrying the system from the initial state to the final state is called a history. If at each stage in the development of a history the probability densities are correctly sampled and large numbers of histories simulated, information about average measurable macroscopic quantities as well as immeasurable microscopic quantities can be obtained. In situations where the calculated macroscopic quantities agree with measured data the validity of the calculated microscopic quantities can be inferred.

Particle transport algorithms were originally developed for high energy neutron and photon transport for nuclear power reactor applications [1], and have later been modified to include lower energy photons as well as electrons.

Monte Carlo techniques are currently used by scientists in engineering, physics, chemistry, and biology. The success of Monte Carlo calculations in recent years in science and technology is attributable to increases in computer speed, decreases in computer costs, and the availability of general purpose Monte Carlo software packages. Such calculations serve as a means of testing the viability of new theories and new designs before their expensive and often time consuming physical implementation. Additionally, they can be used to study naturally-occurring phenomena which are too dangerous to investigate expe.imentally.

In the context of radiotherapy physics and radiation dosimetry, Monte Carlo calculations require the knowledge of the probability distributions governing individual interactions of electrons and photons in different materials in order to simulate the random trajectories of individual particles. The code may be used to simulate radiation transport through a linear accelerator head assembly and into a patient. By collecting data from several thousands of histories, measurable quantities, such as the dose absorbed in the patient as well as difficult (or even impc ;sible) to measure quantities such as electron contamination or component scatter contribution can be obtained. Moreover, since one is able to track each individual particle and each history is subject to the quantum laws of probability and is therefore unique, it is possible to obtain information about the statistical fluctuations particular to the system studied.

A Monte Carlo code for use in medical physics has four primary components:

(1) *interaction cross-section data for photons and electrons*

(2) *particle transport algorithms*

(3) *geometry*

(4) *simulation data analysis*

The cross-section data and the particle transport algorithms are usually provided as part of the simulation package, while the geometry and data analysis routines are user-written. The cross-section data provides the information about the probability distributions that govern the interactions of photons and electrons of various energies with the medium. Particle transport algorithms sample the cross-section data and select the particle step-size, the new particle direction, the amount of energy lost to the medium during each step, *etc.*, while complying with the laws of physics and the constraints set forth by the user. The user can influence the simulation by defining its geometry and by imposing certain cut-off conditions in each of the regions in the geometry. Whenever a certain condition is met, the user chooses to store some of the particle parameters for later evaluation. This is done through the data analysis subroutine. The methods for performing such simulations and data analyses vary depending on the particular Monte Carlo package used, the needs of the user, and on the user himself.

3. EGS4 / PEGS4 MONTE CARLO CODE SYSTEM

Two popular electron transport approaches are available to medical physicists: ETRANS (Electron TRANSport) originally developed at the National Bureau of Standards by Berger and Seltzer [2] and EGS (Electron-Gamma Shower) originally developed at the Stanford Linear Accelerator Centre (SLAC) by Ford and Nelson [3]. The Monte Carlo calculations discussed in this thesis were performed using the most recent EGS computer code, the EGS4 system which is a coupled photon-electron Monte Carlo code developed by W.R. Nelson, H. Hirayama, and D.W.O. Rogers of SLAC [4] with the PEGS4 (Preprocessor for *EGS4*) cross-section preparation package. A brief discussion of the EGS4 / PEGS4 Monte Carlo system will be provided in this section.

The EGS4 computer code package comes complete with a MORTRAN3 pre-compiler which converts MORTRAN3 computer code into FORTRAN77 code. The package is programmed in the MORTRAN3 language; however, the pre-compiler can be controlled by the programmer so that the user-written sections of the code may be written in either FORTRAN or MORTRAN. The MORTRAN3 language was designed specifically for use by EGS4 by Cook and Shustek of SLAC [5] to facilitate the programming of computer simulations and to make them easier to read. MORTRAN3 also provides the user with macro capability which allows the programmer to easily modify the existing code without introducing bugs to the main program.

3.1. PEGS4

The most important component of Monte Carlo calculations in medical physics is the interaction cross-section data, since it is the interaction cross-sections which govern the outcome of every individual particle step. The EGS4 code is capable of simulating the radiation transport of electrons, positrons, photons, and even pi-mesons in any element, compound, or mixture of elements [4]. The necessary cross-section data used by EGS4 is generated by the PEGS4 preparation package, a stand-alone preprocessing code, from cross-section tables of all the elements with atomic numbers ranging from 1 through 100. The data were provided by Berger and Seltzer [6] and have since been adopted by the ICRU in their Report # 37 [7]. The PEGS4 preparation package constructs piecewise-linear fits over a large number of energy intervals (PEGS4 has a dynamic energy range and is capable of providing EGS4 with cross section data for energies as low as a few keV up to several thousand GeV) of the provided cross-section and branching ratio data and prepares the data specially for use by EGS4.

PEGS4, written in MORTRAN3, requires the user to specify the medium and the energy range for which the cross-section data is to be used and then prepares the data in a form which can be used directly by EGS4 for rapid numerical manipulation. It is necessary to run PEGS4 only once for each of the media data files required by EGS4. Once a medium file is created, provided its energy range is sufficiently large, that medium can be used in any EGS4 simulation.

3.2. EGS4

The EGS system of computer code is a general purpose Monte Carlo package for the simulation of coupled electron and photon transport in an arbitrary geometry for particles ranging in energy from a few keV through several TeV. The EGS code system introduced in 1978 (then called EGS3) was designed to simulate electromagnetic cascades from 0.1 MeV (photons) and 1 MeV (electrons) up to a few thousand GeV in energy. In response to public demand, SLAC implemented various changes to the original code, and extended the energy range of electrons down to 10 keV and of photons down to 1 keV to create an updated Monte Carlo code referred to as EGS4.

As the electron travels through a medium it loses its energy through collisional or radiative processes. A collisional loss occurs when the electron interacts with the atoms of the medium and leaves them in ionized or excited states. Ionizations are accompanied by ejected electrons. If the ejected electron has a sufficient energy, it will travel through the medium and cause further ionizations. An energetic ejected electron as such is referred to as a delta ray. If, however, the electron ejected by a collisional interaction is not energetic, it will deposit all of its kinetic energy locally. A radiative loss occurs when the high energy electron interacts with the nuclei of the medium resulting in the creation and emission of electromagnetic radiation.

A cascade-shower includes the initial particle and all of its progeny as it travels through the medium. During the course of a single shower several different processes occur in nature, and in order to accurately simulate the physical situation all of these processes must be taken into account. The EGS4 code considers bremsstrahlung production, positron annihilation, Molière (e^-e^-) and Bhabha (e^-e^+) scattering, as well as continuous energy loss between successive discrete interactions for electrons travelling through a medium, and Compton scattering, photoeffect and Rayleigh scattering for photons.

3.2.1. Program structure and subroutines. The EGS4 package is divided into several interactive subroutines and block data with a flexible user interface which allows the user freed .n to customize sections of the computer code without having to alter other parts of the program. Most of the difficult physics algorithms are provided as part of the EGS4 package; however, the EGS4 code system requires that the user write a controller program referred to as the EGS user code. A flow-chart of the EGS4 structure is given in Figure 3.1. The figure is divided into two sections, one representing the user-written computer code and the other representing the routines supplied by the EGS4 package. The two sections are very distinct from one another, allowing the user to use the EGS4 package with only a minimum knowledge of the complete code. In fact, it is possible to successfully use EGS4 without any understanding of the physics or the computer programming involved in the simulation.

The user code generally consists of a MAIN routine and the subroutines HOWFAR and AUSGAB and any other subroutines the user requires for the simulation. The purpose of the MAIN routine is to establish the various initial conditions and to provide for two necessary subroutine calls. The first sub-

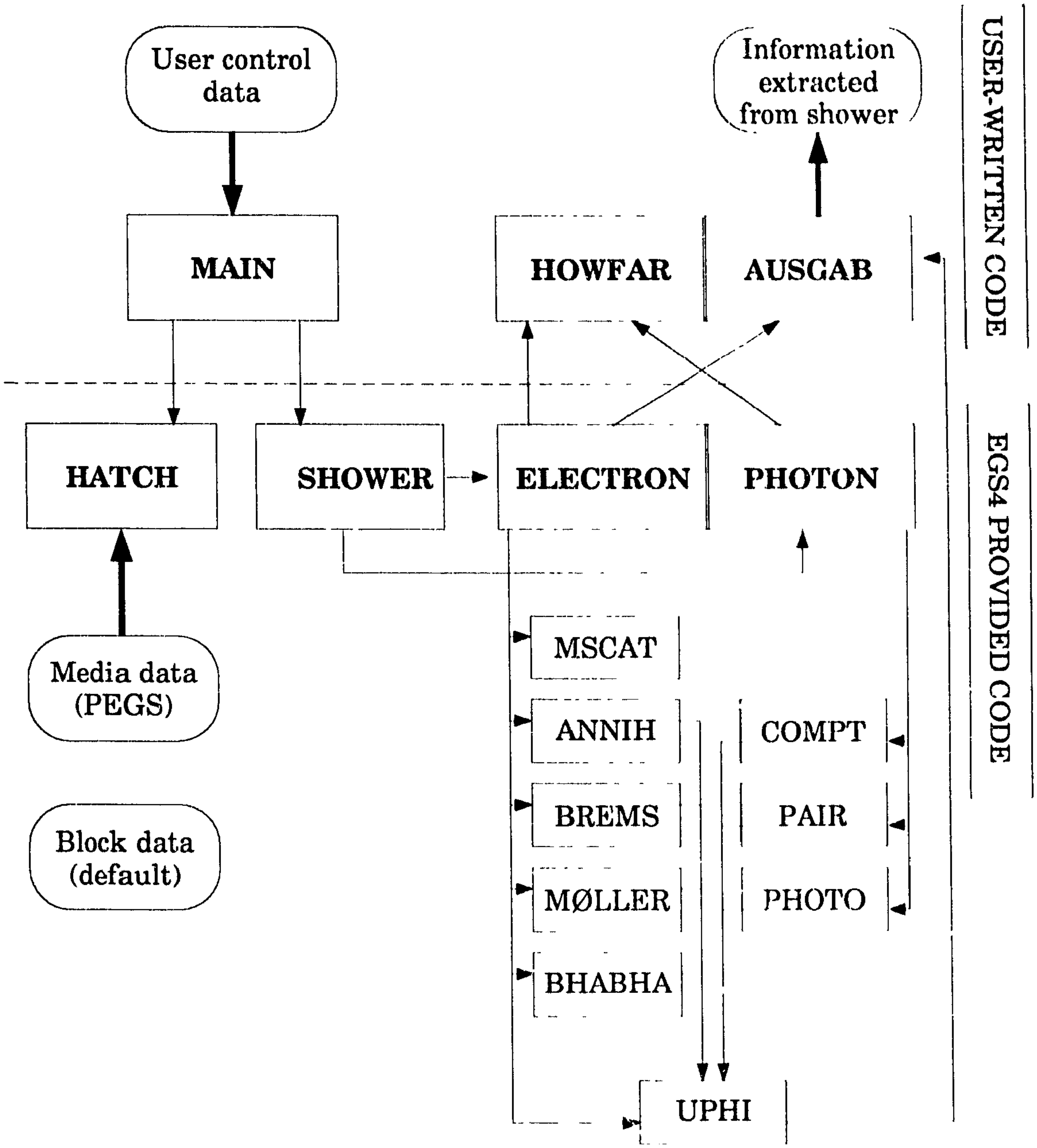

Figure 3.1 Flow chart of the EGS4 Monte Carlo code. The user-written sections of the code are distinct from the provided code. Taken from SLAC report 265 [8].

routine called from the MAIN is the HATCH subroutine. HATCH reads the media data needed for the simulation that was created at an earlier time by PEGS4. The second call is to the SHOWER subroutine which initiates the actual particle transport. SHOWER decides which interaction will occur for either a photon, an electron, or a positron, and then calls the appropriate subroutine which governs the particle transport. After the correct subroutine has been called, subroutine UPHI is called which selects the particle's direction following an interaction. The call to SHOWER can be repeated as many times as required by the user.

Once the desired number of histories have been run, one must analyze and output any information gathered during the simulation. This is done at the end of the MAIN routine. Customarily, the simulation is divided into several batches where each batch is actually a complete simulation of a user-specified number of histories, and the results of each batch are averaged and the statistical variance between the batches is calculated. This gives a measure of the statistical fluctuations of the system and of the error in the computed results.

Whenever EGS4 wishes to transport a particle (via the PHOTON or ELECTRON subroutines), it randomly selects a mean free path distance to the next interaction. Then it calculates the distance to the nearest boundary along the particle's direction. The actual distance that the particle is transported is equal to the smaller of the desired distance and the distance to the nearest boundary. A particle is tracked in this manner until its energy falls below a defined cut-off energy.

The various geometrical regions in the simulation and the medium that occupies each region as well as the equations necessary to calculate the distance to each of the region's bounding surfaces is programmed in the subroutine HOWFAR. Each region has a well defined size, composition, and density. Complex geometries can be represented in terms of blocks of simpler geometries, such as planes, cones, cylinders, and spheres which simplify the programming of the experimental apparatus. In general, programming the exact geometry of the physical situation without the introduction of various simplifications proves to be an excessive burden on the run time of the simulation, and scarcely increases its accuracy. For this reason, a number of geometry subprograms have been created for use within HOWFAR. It is the responsibility of the user to accurately model the geometry of the problem, and at the same time to consider the computation time required for the interrogation of the model by EGS4. The user also defines *discard regions*, i.e., regions which lie beyond the scope of the simulation or which indicate that the particle has reached a region of interest. When a particle reaches a discard region, it is flagged, and the user has a chance to score the particle's properties before they are removed from memory.

The user scores and outputs information about the simulation via the user-written subroutine AUSGAB. By default, subroutine AUSGAB is called by the EGS4 program each time one of the following situations arises:

(1) *a particle step is about to occur,*

(2) *the particle is about to be discarded because its energy is below the cut-off energy,*

(3) *the particle will be discarded because the user requested it in HOWFAR, or*

(4) *a photoelectric interaction has occurred and either:*

a) the energy of the incident photon was below the K-shell binding energy and will be discarded, or

b) a fluorescent photon will be discarded with the K-shell binding energy.

For each of the above circumstances, an argument is passed into the subroutine which indicates the reason for which AUSGAB was called. This is a useful feature of the subroutine which allows the user to score specific events. For instance, if one is interested in the number of times a given electron experiences a photoelectric interaction in a medium, an event counter can be programmed into the AUSGAB subroutine which is incremented each time the subroutine is entered because of a photoelectric interaction. In addition to the above four default conditions, EGS4 allows for another 20 different conditions to interrogate the AUSGAB subroutine. These 20 conditions may be set by the user in the MAIN routine and allow for the scoring of almost any event. The non-default conditions are manually set because they are very job-specific, and if AUSGAB were to be interrogated every time any of the possible situations arose, the simulation time would become astronomical.

3.2.2. Variance reduction techniques. Variance reduction techniques are programming techniques which reduce the time needed to calculate a particular result to within a given uncertainty [9]. Variance and computing time are related by the fact that in order to reduce the variation (error) in calculated results, more histories must be run per simulation, thereby making the simulation more time-consuming. Several techniques that are either electron- or photon-specific are included in the EGS4 package.

As an electron travels through a given geometrical region, it experiences several thousands of interactions with the medium and must undergo a correspondingly large number of transport steps. Each transport step requires that subroutine HOWFAR be called. It becomes very time-consuming if after every step the distance to the nearest bounding surface is calculated. An alternative used by EGS4 is to determine the distance to the nearest boundary once and then to decrement this variable by the length of each transport step. It would be impossible for the particle to cross a bounding surface while the distance variable is greater than zero, therefore the geometry subroutines found in HOWFAR are not called. If the distance variable becomes equal to or less than zero, the geometry subroutines must be interrogated and the distance variable is recalculated. For electrons, which experience very small step sizes, this technique greatly reduces the number of times the HOWFAR subroutine is called and avoids unnecessary program run-time.

The accuracy of all electron transport codes depends on the electron step sizes. In general, the shorter the step sizes the fewer the approximations and the greater the accuracy. However, a reduction in the electron step sizes incurs a proportional increase in the number of calculations performed and thus a corresponding increase in the overall computing time. A second electron-specific variance reduction technique employed by EGS4 attempts to select the optimum electron step sizes to balance accuracy and computation time. The PRESTA transport algorithm (parameter reduced electron-step transport algorithm) was developed by Bielajew and Rogers in 1986 [10]. The PRESTA algorithm is capable of selecting the electron step size depending on the location of the particle and the composition of the transport medium. Far away from boundaries, PRESTA allows large electron steps to occur, while only small steps are permitted near boundaries or interfaces between media. This eliminates the problem of selecting the electron step size by the user and ensures reliable results while saving computation time, since large steps can be used far away from boundary surfaces.

In some instances, the probability of a desired event is very low, consequently the variance in the calculated results is very high. In order to obtain results which are statistically valid, the number of occurrences of this event must be increased. One can either increase the total number of histories to be run, or one can apply a *particle splitting* technique. For instance, if one is interested in the distribution of the electron contamination to within 2% error produced by a medical linac, but the contamination constitutes less than 1% of the total number of the total particle flux and the uncertainty in the measurement is ± 10%, then the occurrence of electrons must be increased by roughly

25 times, since the uncertainty is proportional to the inverse root of the number of events. If the original simulation takes 1 day to complete, then to achieve 2% accuracy, the simulation must be run for 25 days, or each time an electron is produced with an energy above a given threshold it may be multiplied 25 times. The statistical significance of each of the 25 new electrons must then become 1/25th the significance of the original particle in order for the overall probability of the occurrence of an electron to remain equal to 1. Each new electron is then treated as any other particle and the simulation continues onward from that point only now with 25 electrons to follow instead of only the 1 electron. This technique will reduce the variance in the electron flux enough to bring the error down to 2% while increasing the simulation time only by approximately 2.4%.

4. THEORETICAL CALCULATIONS

The process of simulating the dose deposition as a function of the depth in a tissue-equivalent phantom must be divided into different sections for the simulation to be time-efficient. The division of the total simulation into smaller subsections increases the overall speed and flexibility of the computations. Consider that it takes 10 million electrons incident on the x-ray target to generate 15 thousand photons which reach the patient, taking 1 day of computer time to do it. It is necessary that 1 million photons enter the patient in order for the dose delivered to the patient to be calculated with an uncertainty of the order of ± 5%. Thus, if the simulation of the Clinac-18 treatment head and the simulation of the patient were combined into one program, it would take 67 million incident electrons to produce doses having uncertainties of ± 5% (this would take 67 days per simulation).

The initial stage in the Monte Carlo calculations of the percent depth dose along the central axes of various field sizes for the Clinac-18 linac involves the modelling of the Clinac-18 itself. After designing a sufficient model to represent the Clinac-18, calculations of the output spectra of particles and their energies for various field sizes are performed. Later, a spectral analysis program is used to analyze the data and prepare it for later use by the next stage of the simulation. The final step involves the simulation of the irradiation of a water phantom with the spectra from the various field sizes. This is accomplished by sampling the spectral data in order to select each individual particle incident on the phantom and then following the particles transport through the phantom and calculating the energy it deposits at each depth.

4.1. Clinac-18 treatment head

The actual dimensions of the Clinac-18 treatment head are provided courtesy of Varian Oncology Systems [11]. The Clinac-18 treatment head design is simplified and various cones, cylinders and planes are used to represent this simplified model.

Figure 3.2 demonstrates how this simplification technique is applied to the actual linac design. The figure shows a typical complex flattening filter shape and the simplified model used to represent it in the program. The actual flattening filter (Fig. 3.2 (a)) can be represented in several ways. Figure 3.2 (b) shows the flattening filter modelled with a series of concentric cylinders piled one on top of the other. This method was regularly used in the past before an algorithm for the modelling of cones was developed. Presently, it is possible to model the same flattening filter with fewer sections and greater accuracy with a series of conical segments as shown in Figure 3.2 (c).

The simulations of the Clinac-18 treatment head are performed assuming that a pencil beam of electrons each having a kinetic energy of exactly 10 MeV is directly incident on a uniform density copper target. Both the photons produced in the target and the electrons escaping the target and all of their progeny are followed until they exit the region of interest (if a particle scatters far enough laterally that the likelihood of it or any of its progeny reaching the primary field is small, it is discarded), until their energy drops below a cut-off energy (each material used in the simulation has a different cut off energy) or the particles cross the scoring plane (located 100 cm from the copper target). If a particle crosses the scoring plane, its energy, location, direction, and the region where it was created along with the region from which it last scattered is output to a file. In this way, the data can be manipulated and analyzed independently of the simulation at a later time by the programmer.

In order to increase the speed of the simulation and insure good counting statistics, a few variance reduction techniques are used in the simulation. One technique used in the Clinac-18 treatment head simulation is *electron*

(a)

(b)

(c)

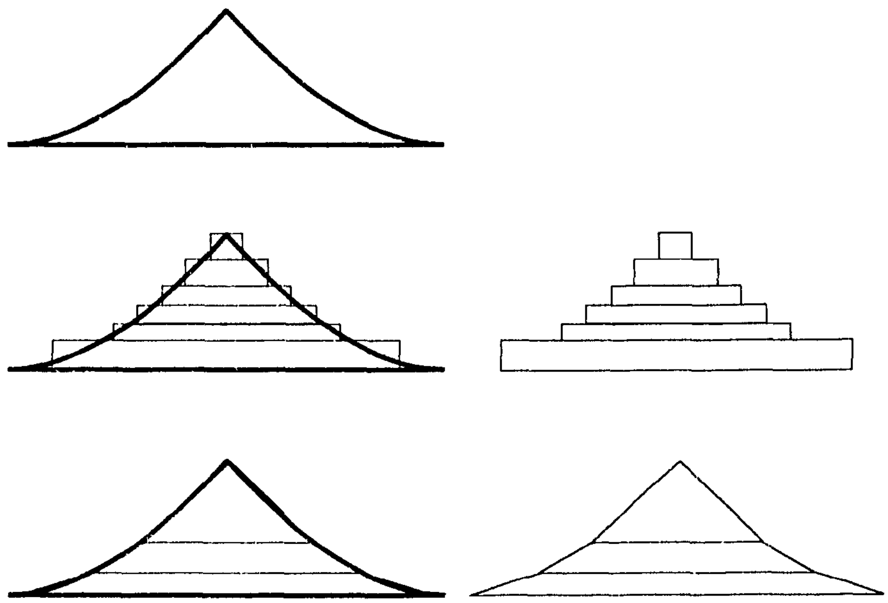

Figure 3.2 Schematic representation of the complex geometry of a typical flattening filer (a), and how it can be modelled with a series of simple geometric shapes. (b) The flattening filter is modelled using six concentric cylinders. (c) Three cones are used to model the flattening filter. Three cones provide a more accurate representation of the actual flattening filter geometry than do six cylinders.

splitting. Whenever an electron is created, it is divided into 10 new electrons having 1/10th the statistical weight of the parent particle. Then each of the 10 electrons is followed separately from that location until it is discarded. Since the relative photon fluence is very high for most of the simulations, a time reduction technique is used to make the simulation run faster without reducing the statistical accuracy of the photon parameters. Prior to a photon reaching the collimating jaws, a game of Russian roulette is played. The computer generates a random number between 0 and 1 and compares it to a predefined number (the survival probability). If the computer-generated random number is less than the survival probability, the photon loses the game and is discarded. If, however, the random number is greater than the survival probability, the photon wins and is allowed to continue. To ensure that the overall probability of a photon to cross this imaginary plane is equal to 100%, the surviving particles are given a weighting of 1/(survival probability). The survival probability should be large enough that the statistical fluctuations in the quantities carried by the photons are not significant in the final calculated results. Due to programming difficulties which have since been resolved, the PRESTA electron transport algorithm was not implemented at this first stage of the Monte Carlo simulations. The cut-off energies for electrons were 0.8 MeV in air, 1.0 MeV in the target and flattening filter, and 2.0 MeV in the tungsten and lead shielding.

4.2. Spectral analysis

The data produced by the simulation of the Clinac-18 treatment head is analyzed by a completely independent program. This allows for greater flexibility of the analysis program because the data can be analyzed in several different ways. It also acts as a time saving technique because analyses not considered at the time of the original simulation can be performed without repeating the entire simulation. If the data analysis were written as part of the simulation program, the simulation would have to be repeated for each new analysis.

The spectral analysis program calculates the photon densities in different annular regions centered on the beam axis and the corresponding photon energy distributions in each region. It also calculates the electron energy distribution of the entire radiation field. Electrons, unlike photons, cannot be analyzed according to region because their numbers are too low. Theoretically, electrons reaching the scoring plane will have undergone numerous scattering processes and will be evenly distributed across the treatment field, therefore, electron parameters of all the regions are grouped together. The calculated photon and electron distributions act as the radiation sources which are sampled by the DOSRZ program for calculation of the dose deposited in a phantom for the different field sizes.

The program also calculates the average energy and the average direction cosine per annular region of the photons which reach the scoring plane, and the total electron contamination. A breakdown of the percentage and average energy of the photons and electrons reaching the scoring plane that were created or scattered in the primary collimator, the flattening filter, the ionization chamber, the lead shield, the tungsten shield, the collimating jaws, or in the air between the x-ray target and the patient is also given by the analysis program.

4.3. Calculating the dose in the phantom

The dose deposition in a water phantom is calculated using the DOSRZ cylindrical dose scoring program supplied as a part of the EGS4 Monte Carlo package. The program was modified to include electron contamination as part of the initial particles set in motion in the phantom. Modifications were also necessary to allow for the sampling of the energy distributions of the particles as a function of the particle's radial position. Incident particles are sampled from the probability distribution prepared by the spectral analysis program and then the particle charge is determined. If the particle is a photon, its energy is determined by sampling the photon radially-dependent energy spectrum, otherwise the electron energy distribution is sampled. The incident particle is assumed to come directly from a point source located in the x-ray target. The cut-off energies were chosen to be 0.030 MeV for photons and 0.550 MeV for electrons (total energy). The number of incident particles was selected to provide a smooth PDD curve in the phantom.

The DOSRZ program takes advantage of cylindrical symmetry by dividing the phantom into several cylindrical regions and scoring interaction events as a function only of the particle's radial distance from the central axis and its depth in the phantom. Its simple geometric structure allows for the efficient use of the PRESTA algorithm. For studies along the central axis of the beam, this approach is sufficient, however, near the edges of the field, the symmetry is broken and edge effects become important. Because this study is interested in the PDD curve along the central axis, the DOSRZ should provide reliable results for all but the smallest of fields.

The build-up region is divided into 30 regions each having a depth of 1 mm. Beyond the build-up region, the depths of each region are gradually incremented to 1 cm down to a depth of 21 cm. The depth doses are calculated only in the region located around the central axis to save computation time. The results are output to a file in the form of a two-dimensional array for later analysis.

5. REFERENCES

1. D.W.O. Rogers, A.F. Bielajew: *Monte Carlo techniques of electron and photon transport for radiation dosimetry*, in: The dosimetry of ionizing radiation, vol. 3, K.R. Kase, B.E. Bjärngard, F.H. Attix (eds.). Academic Press, San Diego, California (1990), pp.427-540.

2. M.J. Berger, S.M. Seltzer: *ETRAN, Monte Carlo code system for electron and photon transport through extended media,* Documentation for RSIC computer dose package CCC-107, Oak Ridge National Laboratory, Oak Ridge, Tennessee (1973).

3. R.L. Ford, W.R. Nelson: *The EGS code system (Version 3)*, SLAC report 210, Stanford Linear Accelerator center, Stanford, California (1978).

4. W.R. Nelson, H. Hirayama, D.W.O. Rogers: *The EGS4 code system*, SLAC report 265, Stanford Linear Accelerator center, Stanford, California (1985).

5. A.J. Cook, L.J. Shustek: *EGS4 User guide to Mortran3*, SLAC report 265, Stanford Linear Accelerator center, Stanford, California (1985).

6. M.J. Berger, S.M. Seltzer: *Stopping powers and ranges of electrons and positrons*, NBS report NBSIR 82-2550-A (1983).

7. ICRU report # 37, *Stopping powers for electrons and positrons*, International Commission on Radiation Units and Measurements, Washington, DC (1984).

8. W.R. Nelson, H. Hirayama, D.W.O. Rogers: *EGS4 flow diagrams*, SLAC report 265, Stanford Linear Accelerator center, Stanford, California (1985).

9. A.F. Bielajew, D.W.O. Rogers: *Variance reduction techniques, in:* Monte Carlo transport of electrons and photons, T.M. Jenkins, W.R. Nelson, A. Rindi (eds.), Plenum Publishing Co., New York, (1987), pp.407-419.

10. A.F. Bielajew, D.W.O. Roges: PRESTA: *The parameter reduced electron-step transport algorithm for electron Monte Carlo transport*, Nuc. Instr. Meth. Phys. Res. **B18**, 165 (1987).

11. Private communication with Calvin Huntzinger, Varian Oncology Systems, Varian Associates, Inc., Palo Alto, California.

CHAPTER 4
RESULTS AND DISCUSSION

1. INTRODUCTION

A computerized model of the Clinac-18 treatment head was used to calculate the beam characteristics of the linac operating in the 10 MV x-ray mode for various field sizes. The photon energy spectra produced by the Clinac-18 linear accelerator for each field size were calculated, and the scatter contribution to each treatment beam was analyzed. The average photon energy and the percent electron contamination as functions of the field size were also investigated.

The calculated photon energy spectra and the electron contamination data were used to provide the radiation source input for the EGS4-package DOSRZ dose-scoring routine which was used to calculate the percent depth dose (PDD) in water for each field. The Monte Carlo calculated PDD data are compared to measured PDD data in order to test the validity of the theoretical model. Agreement between measured and calculated data implies that the calculated spectra are accurate and is, therefore, critical to the acceptance of the calculated results.

Percent depth doses for various field sizes were measured with both solid and liquid tissue-equivalent phantoms. A radiation field-analyzer with semiconductor detectors was used to measure the PDD in water to a depth of 250 mm and a polystyrene phantom was used in conjunction with an end-window parallel plate ionization chamber to measure the dose deposition in the build-up region. The measured data are compared with results published by other researchers.

2. MONTE CARLO CALCULATIONS OF THE PHOTON SPECTRA

The Monte Carlo calculations of the Clinac-18 photon spectra for square treatment fields ranging in size from 2×2 cm^2 to 20×20 cm^2 were performed by following the trajectories of particles produced by a pencil beam of monoenergetic 10 MeV electrons incident on a thin copper target as they subsequently travelled through the various components of the linac treatment head. The energy, position, direction, and charge along with other characteristics of each particle that crossed the scoring plane at a source-surface distance (SSD) of 100 cm was stored for future analysis.

The calculated photon spectra, produced by the Clinac-18 in its normal operational x-ray mode (with the flattening filter), were used as the particle data for the DOSRZ program and are shown in Figure 4.1 for field sizes ranging from 2×2 cm^2 to 20×20 cm^2. All photons reaching the scoring plane inside the treatment field as defined by the collimating jaws were included in the calculations of the photon spectra. The total x-ray beam spectrum is made up of two separate components: the primary spectrum and the scatter spectrum. The primary photon beam is defined as the portion of the total beam which has

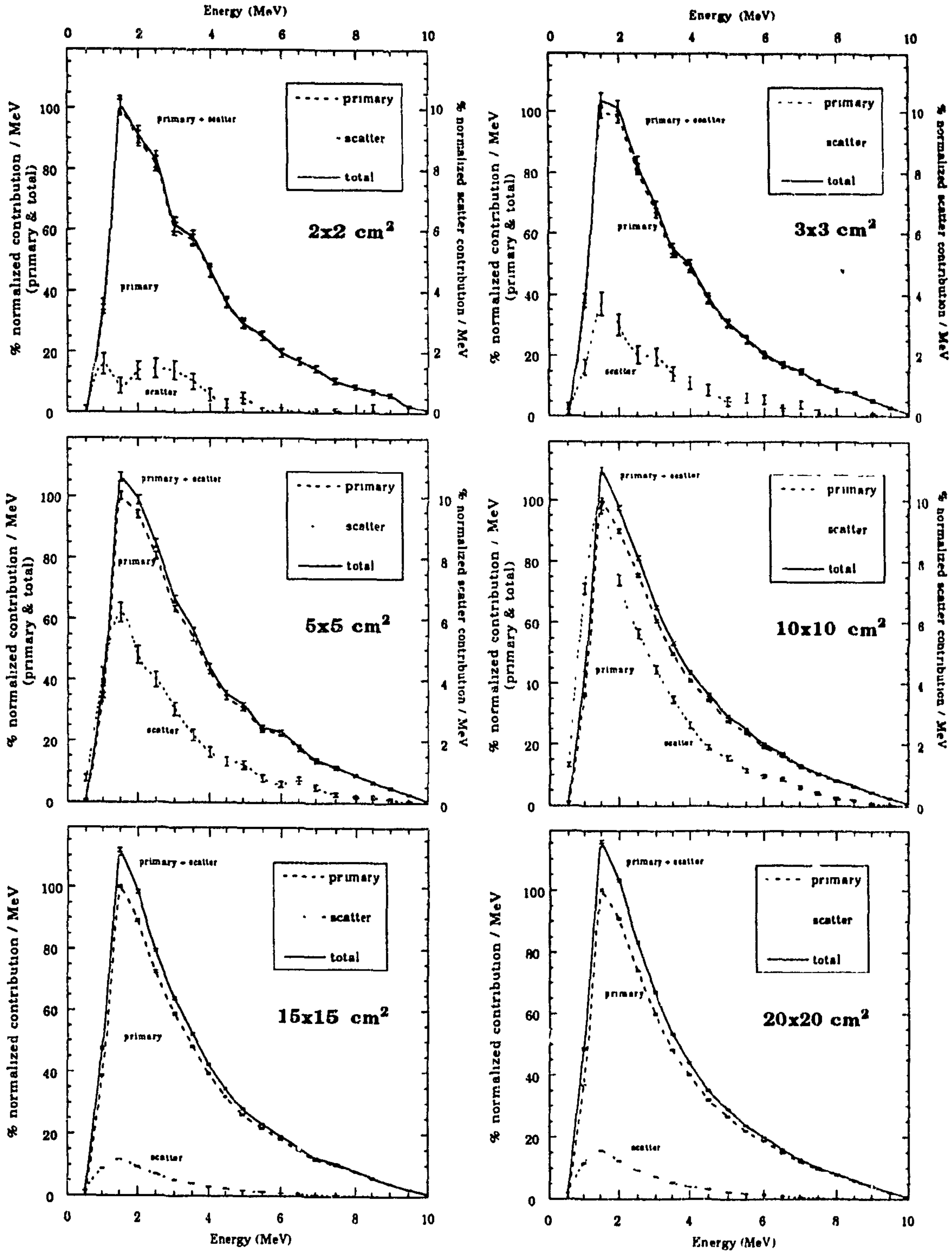

Figure 4.1 Calculated photon energy spectra for various field sizes produced by the Clinac-18 operating with the flattening filter. The scatter contribution is magnified by 10 for fields of 10×10 cm^2 and smaller.

not been scattered by any components of the treatment head, while any particle which has interacted with any component of the treatment head (including air) other than the x-ray target makes up the scatter spectrum. The spectra shown in Figure 4.1 are normalized to 100 for the maximum in the spectrum of the primary photon beam for each field. In order to better view the scatter contribution for small fields, a magnification of 10 is applied to the scattered photon data for fields smaller than 15×15 cm^2 in size.

It is evident from Figure 4.1 that the primary and scatter components of the spectra depend on the field size, and that the calculated spectra become smoother with increasing field size as a result of an improvement in the counting statistics. The increase in the scattered photon contribution to the x-ray beam is quite noticeable as the collimating jaws are opened. Scatter accounts for only 1.5% of the overall treatment beam for the 2×2 cm^2 field as compared to 11.5% of the beam for the 20×20 cm^2 field, implying that for small fields, most of the scatter produced in the treatment head is blocked by the collimating jaws. This result is not surprising since the amount of radiation passing through the opening in the collimating jaws is proportional to the solid angle of the opening as viewed by the photon source. The components of the treatment head from which scatter is likely to arise are located away from the central axis (with the exception of the flattening filter and the ionization chamber), thus the solid angle made by the opening of the collimator jaws as viewed by such components is small compared to that of the x-ray target. However, since the scatter-causing components are located closer to the collimating jaws than the x-ray target, the solid angle subtended by the collimating jaw opening with respect to the scatter components increases faster with increasing jaw opening than does the solid angle with respect to the x-ray target. In other words, the scattered photon contribution to the total treatment beam is more sensitive to changes in the size of the collimating jaws opening because of their proximity to the jaws.

During the Monte Carlo simulation of the Clinac-18 treatment head, the treatment head component in which each particle was created and the component in which its last interaction occurred was recorded. An analysis of these two factors reveals the probability that a particular component of the treatment head influences the scattered photon contamination reaching the patient. If the probability that a particle is created in the jth component is C_j and the probability that a particle is scattered last in that component is S_j then the total probability that a particle interacts with a given component is given by P_j where,

$$P_j = C_j + S_j - C_j \bullet S_j \tag{4.1}$$

A plot of the probability that a given component influences a photon reaching the scoring plane as a function of the field size is given in Figure 4.2 which shows that the flattening filter is the most significant scattering component in the linac treatment head; all other components are between one and three orders of magnitude less significant.

In Figure 4.3 (a), the primary beam photon spectra of Figure 4.1 which reach the scoring plane for the different field sizes are plotted together. The

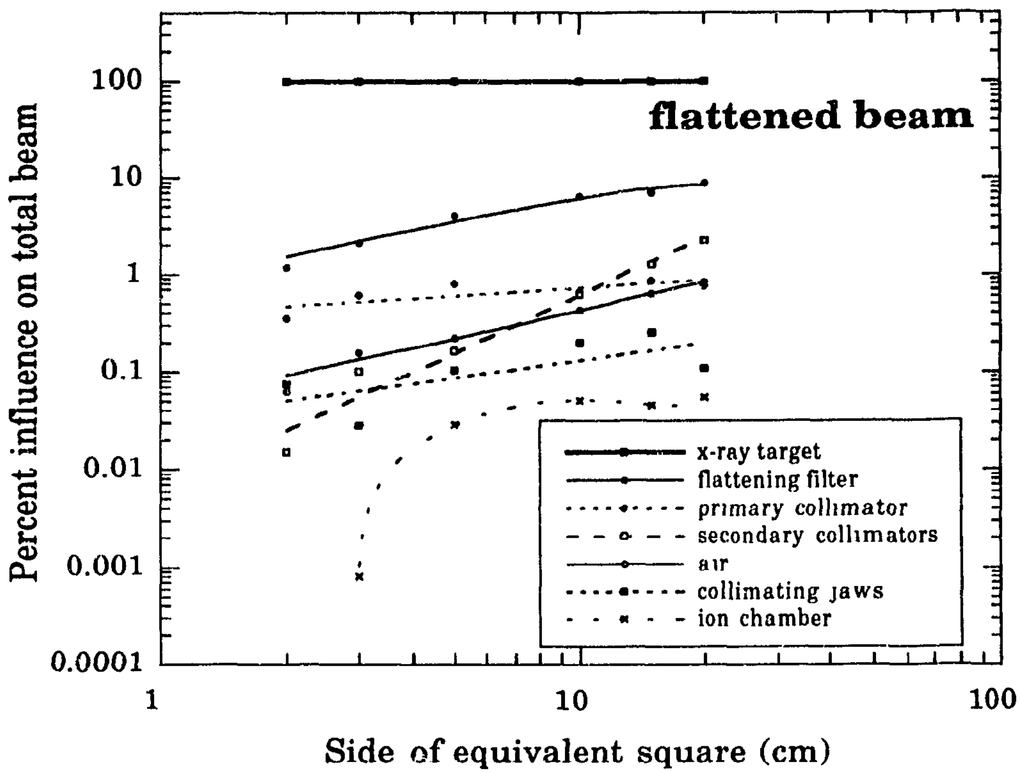

Figure 4.2 The probability that a given treatment head component influences the photon spectrum at the scoring plane (SSD=100 cm) as a function of the field size. The most significant scatter producing component is the flattening filter.

primary photon spectrum becomes softer (less energetic) with increasing field size, indicating that as the field size increases the relative number of high-energy photons making up the primary x-ray beam decreases. This can be explained by considering the shape of the x-ray flattening filter. Since the flattening filter thickness decreases as one moves away from the central axis, the ability of the flattening filter to attenuate the primary beam is lower at its periphery than at its centre. This means that fewer low-energy photons will be removed from the primary beam at wide angles with respect to the central

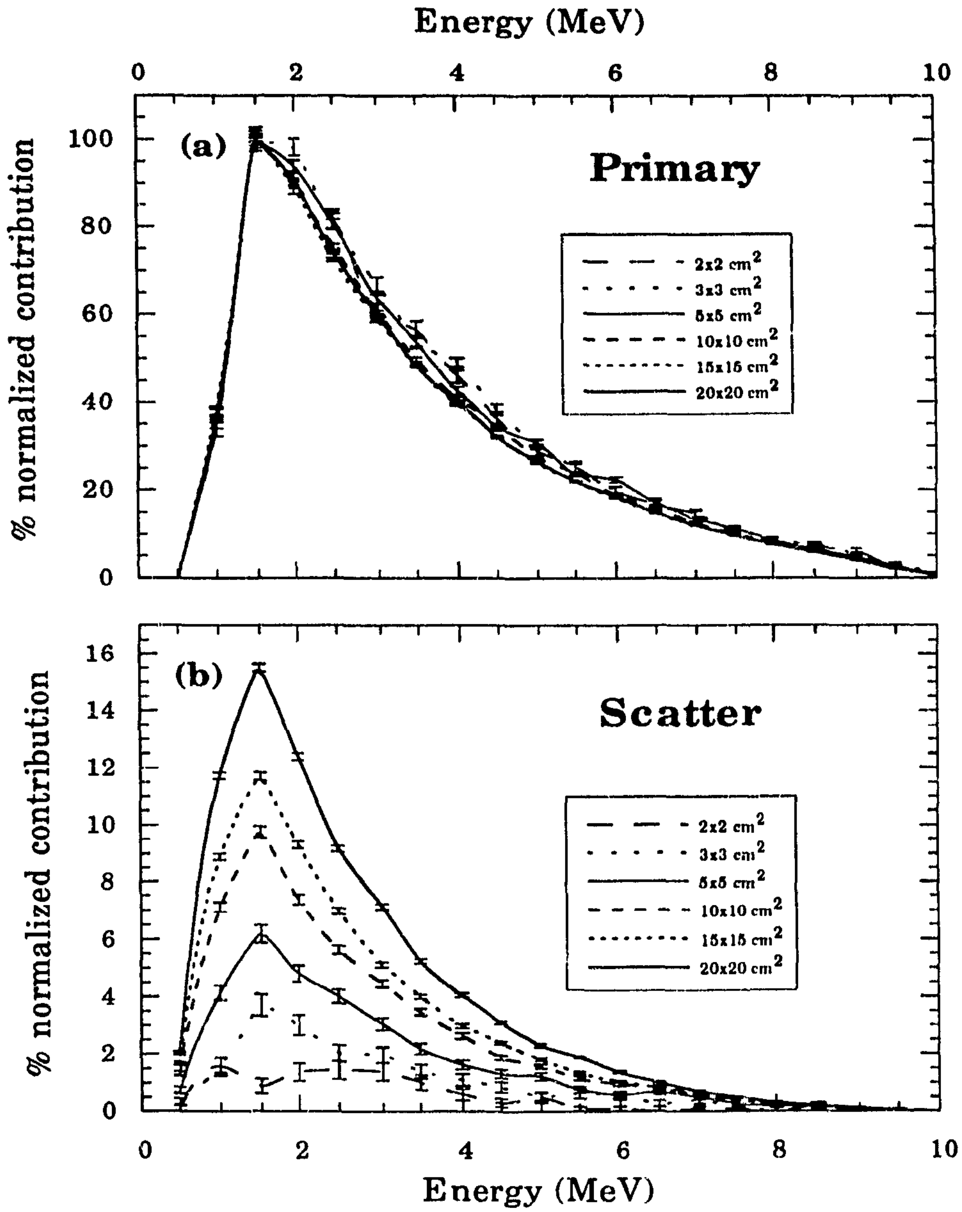

Figure 4.3 Comparison of the flattened x-ray beam primary (a) and scatter (b) photon energy spectra for different field sizes. The primary x-ray beam experiences a decrease in the high-energy components as the field size is increased. The scatter contribution to the flattened treatment beam increases as the field size is increased.

axis, hence more low-energy photons will make up the primary beam. As the field size is increased, the number of off-axis photons reaching the scoring plane is increased along with a correspondingly higher relative contribution of low-energy photons. The net effect is to reduce the relative contribution of the high-energy photons in the primary beam, i.e., the effective energy of the photon beam in off-axis directions is lower than that on the central axis. The same effect is not expected to occur in the unflattened beam, however, an imperceptible decrease in the relative contribution of high-energy photons to the unflattened photon energy spectrum is expected due to the forward energy-peaked nature of the bremsstrahlung scattering process in the x-ray target.

The scattered photon spectra of Figure 4.1 for the different field sizes are plotted together in Figure 4.3 (b). In this plot, all of the scatter contributions are shown with the same scale, making it evident that the amount of scatter increases with increasing field size.

In order to simulate the x-ray beam of the Clinac-18 treatment head without the photon beam flattening filter, the original simulation program was modified slightly and the tungsten flattening filter of the original simulation was replaced by an air flattening filter, effectively removing the flattening filter from the treatment head. The data calculated for the unflattened beam is treated identically to the procedure outlined above for the flattened beam. Figure 4.4 shows the energy spectra of photons reaching the scoring plane when the flattening filter is replaced by air. Because the scatter contribution to the unflattened x-ray beam is very small, all graphs show the scatter

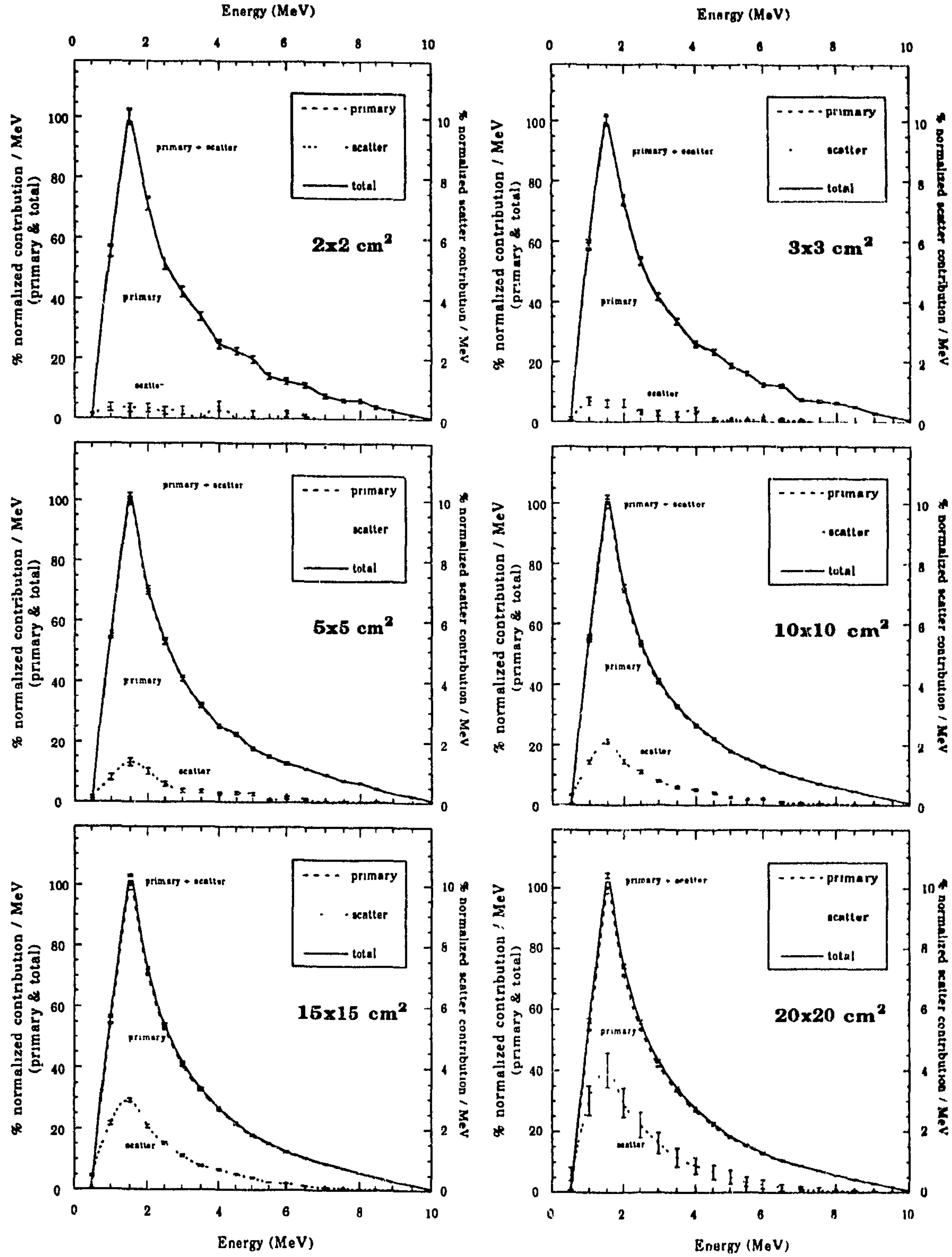

Figure 4.4 Calculated photon energy spectra for various field sizes produced by the Clinac-18 operating without the flattening filter. The scatter contribution is magnified by a factor of 10 for all fields.

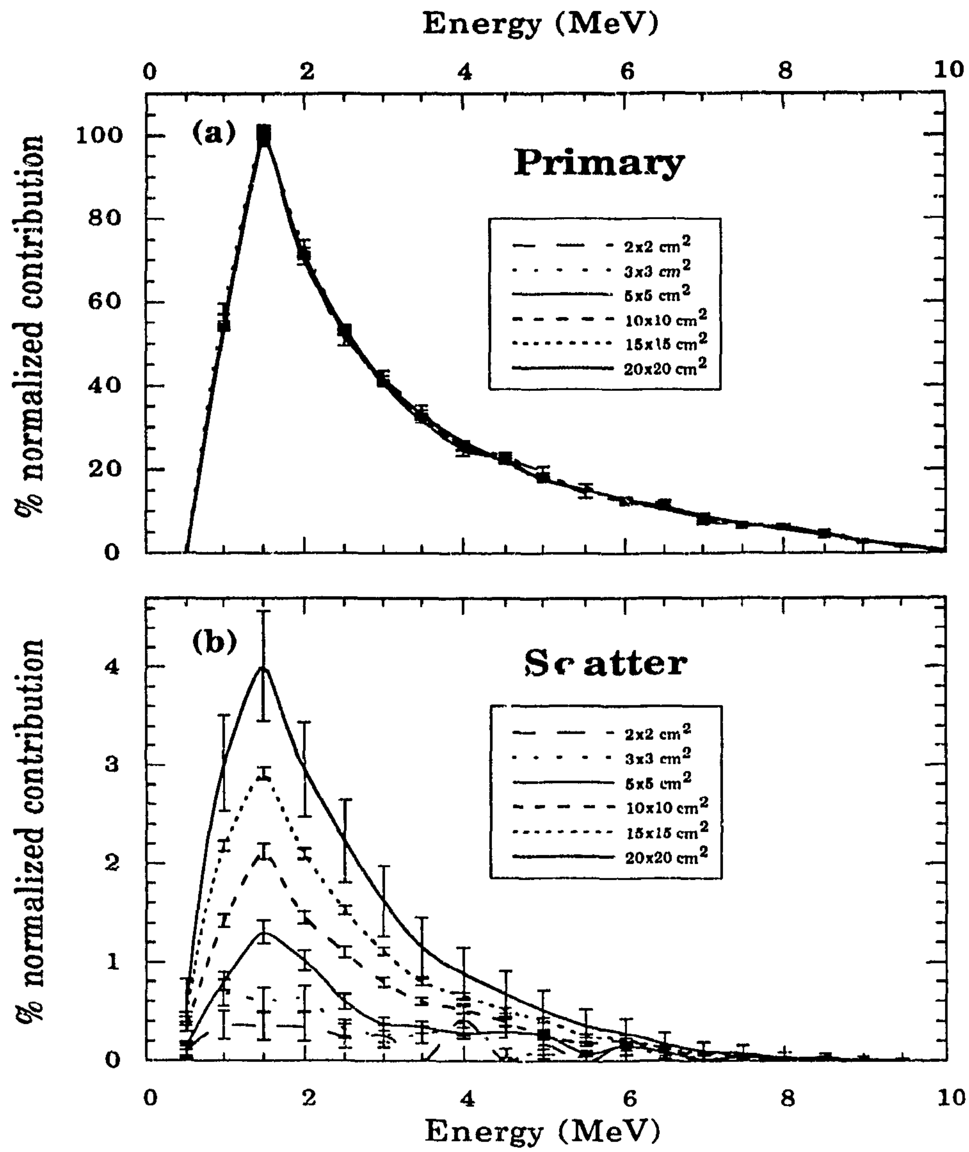

Figure 4.5 Comparison of the unflattened x-ray beam primary (a) and scatter (b) photon energy spectra for different field sizes. There is no change in the primary contribution as the field size is increased. The scatter contribution to the total beam increases with increasing field size. Comparison with Figure 4.3 (b), howerver, reveals that the amount of scatter present in the flattened beam is four times greater than that of the unflattened beam.

component magnified by a factor of ten. Again the primary photon spectra become smoother with increasing field size due to an improvement in the counting statistics. The magnitude of the scatter contribution to the x-ray beam without the flattening filter, although much less than the scatter contribution with the flattening filter, also increases with increasing field size, as expected.

In Figure 4.5 (a), the unflattened primary photon beam spectra of Figure 4.4 are plotted together. The primary photon beam does not become noticeably softer with increasing field size because the beam is equally attenuated at every angle with respect to the central axis. The scatter contribution to the total x-ray beam, shown in Figure 4.5 (b), increases with increasing field size; however, the amount of scatter is significantly reduced when no flattening filter is present, and the scatter accounts for only 3.5% of the total treatment beam for the largest field of 20×20 cm^2.

The influence of each treatment head component on the x-ray beams produced without the beam flattening filter, calculated according to Equation 4.1, is plotted in Figure 4.6 as a function of the field size. A comparison with Figure 4.2 reveals that the relative contribution of each component to the scatter profile is the same whether or not the flattening filter is in place. There is, however, a noticeable increase in the influence of air-scattered photons on the total beam which can be attributed to two effects. Firstly, the region previously occupied by the flattening filter is now replaced by air, hence there is a greater volume of air in which scatter is produced. Secondly, a larger

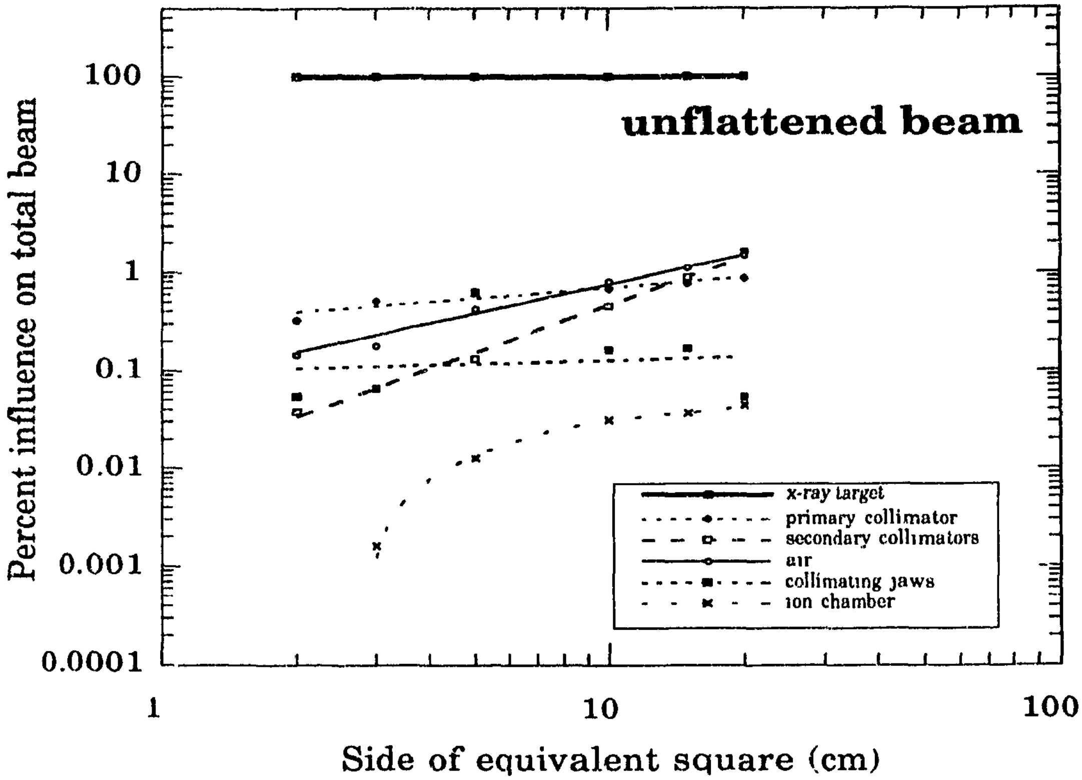

Figure 4.6 The probability that a given treatment head component influences the photon spectrum at the scoring plane (SSD=100 cm) as a function of the field size for the unflattened 10 MV x-ray beam.

number of photons which are scattered in the air above the flattening filter are able to reach the scoring plane as they are not attenuated in the filter when the filter is not present.

The photon energy spectra produced in the Clinac-18 operating with and without the beam flattening filter in place are compared in Figure 4.7. Parts (a) and (b) show the primary photon energy spectra for a 2×2 cm^2 field and a 20×20 cm^2 field, respectively. In both cases, the flattened primary beam is harder than the unflattened primary beam. There is a greater relative con-

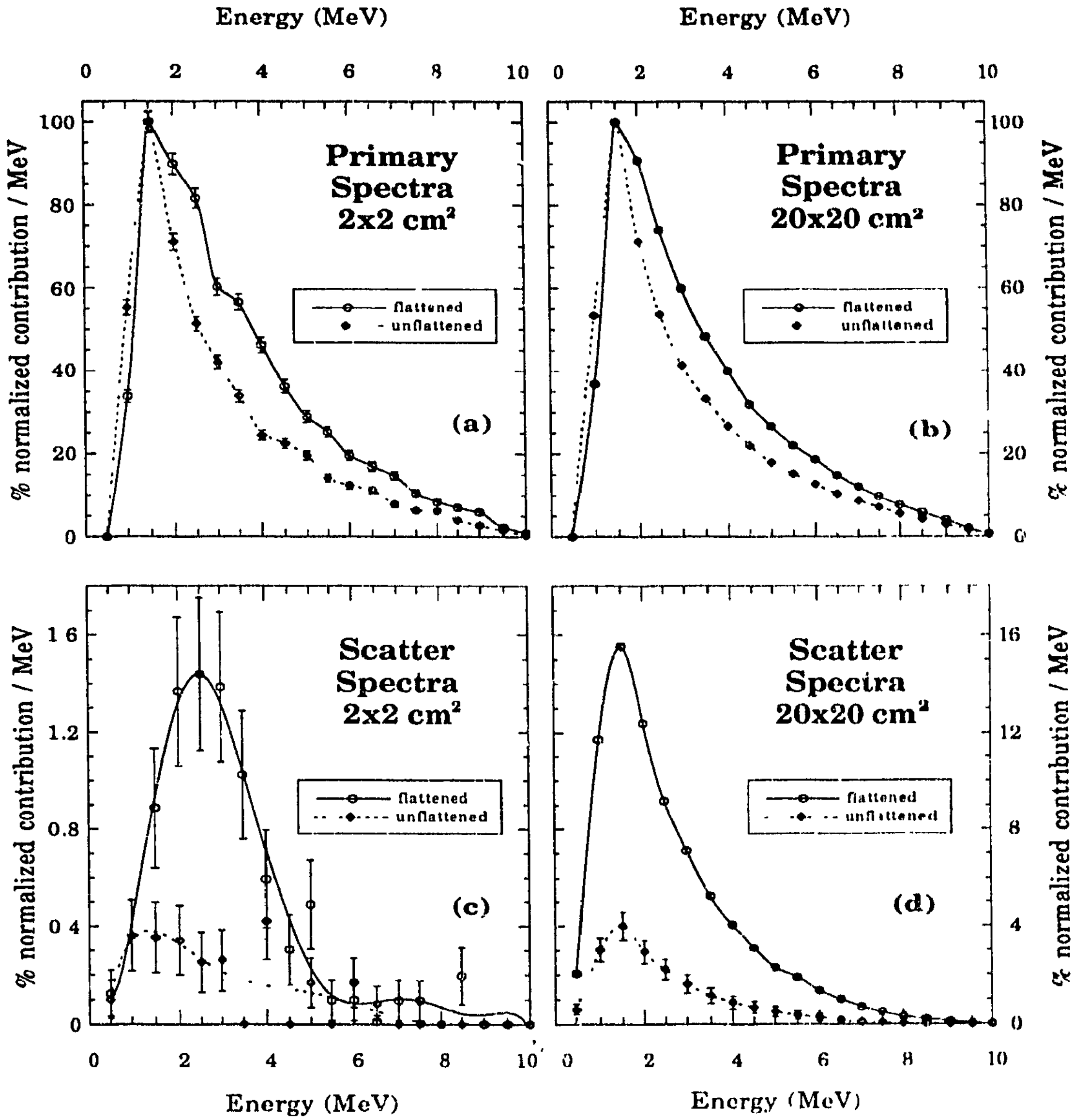

Figure 4.7 Comparison of the flattened and unflattened contribution of the primary photon beams for a 2×2 cm^2 field (a) and a 20×20 cm^2 field (b). In both cases, the flattened beam has a greater percentage of high-energy photons than the unflattened beam. The scatter contribution for a 2×2 cm^2 field and a 20×20 cm^2 field are shown in (c) and (d), respectively. The scatter component of the flattened beam is approximately four times greater than the scatter component of the unflattened beam.

tribution of high-energy photons in the flattened beam along with a smaller contribution of low-energy photons. For this reason the flattened beam will be more penetrating than the unflattened beam for a given field size. In Figures 4.7 (c) and (d) the scattered photon contribution is shown for the 2×2 cm^2 and the 20×20 cm^2 fields, respectively. It is important to note that for both field sizes the scatter contribution for the flattened beam is 4 times greater than that for the unflattened beam. This large amount of scatter in the flattened photon spectra at large field sizes degrades the quality of the x-ray beams because it greatly adds to the low-energy components of the beams. This will lead to an increased dose in the build-up region as well as a lower depth of dose maximum (d_{max}) with increasing field size since low-energy photons are much less penetrating and more prone to large-angle scattering in water than are high-energy photons.

The calculated mean photon energies of the flattened and unflattened treatment beams as functions of the field size are shown in Figure 4.8. The mean photon energy was calculated from the raw simulation data by integrating the total amount of energy carried by all of the photons forming the entire treatment beam and dividing by the total number of photons in the beam. It is evident that the average energies of both the primary and the total x-ray beams decrease with increasing field size for the flattened x-ray beam, while for the unflattened beam, the average photon energies decrease only slightly with an increase in the field size. The mean energies of the total x-ray beams decrease at a faster rate than the mean energies of the primary beams in both situations. The reason for this is that the total beam includes low-energy scattered photons whose numbers increase with increasing field size. The large amount of low-energy scattered photons which contribute to the total x-ray beam for large fields leads to an increase in the dose in the build-up region which may be significant enough to cause a decrease in d_{max}.

The electron contamination as a percentage of the total of the flattened and unflattened treatment beams are also calculated as functions of the treatment field size and the influence of the flattening filter on the electron contamination is investigated. In Figure 4.9, the percent electron contamina-

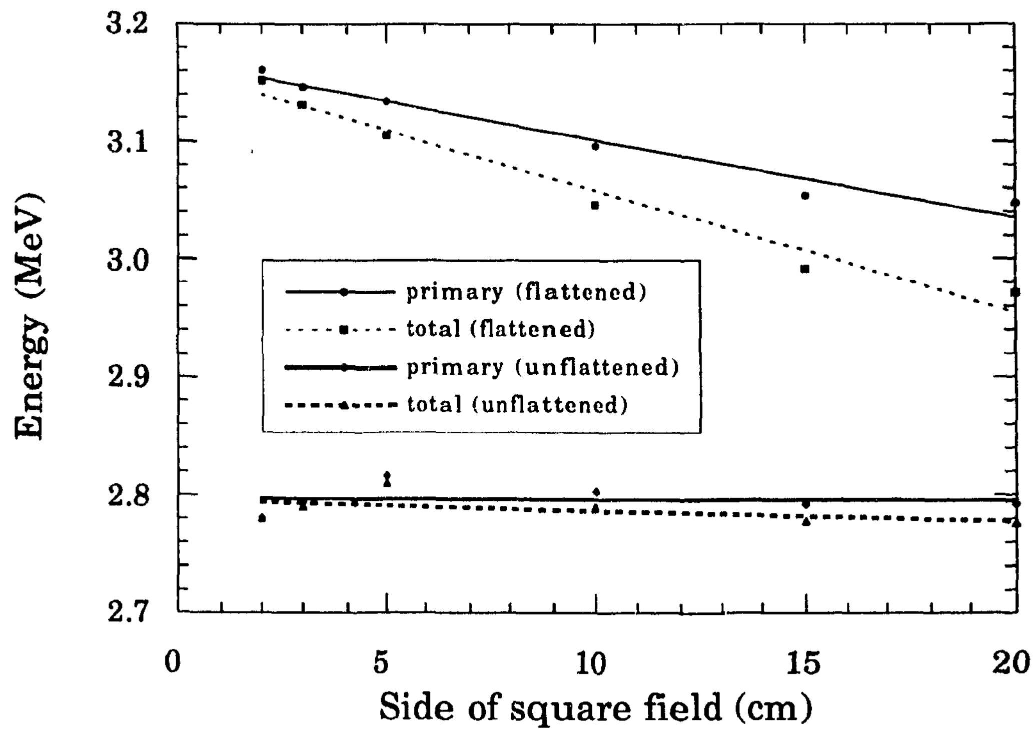

Figure 4.8 Mean energy of the primary and total x-ray beams as a function of the field size for the flattened and unflattened Clinac-18 10 MV x-ray beam.

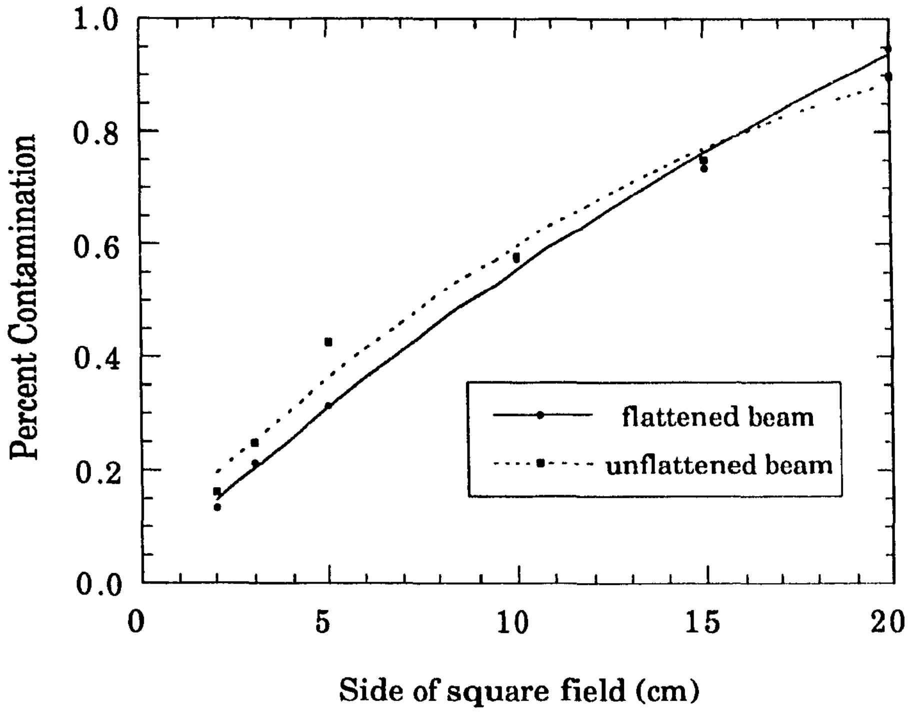

Figure 4.9 Percent electron contamination of the flattened and unflattened Clinac-18 10 MV x-ray beam as a function of the field size. The electron contamination with and without the flattening filter are approximately equal and increase with increasing field size.

tion as a function of the field size for both the flattened and the unflattened beam are plotted. For the same field size the electron contribution is roughly equal for both the flattened and unflattened beams indicating that the flattening filter is not a major source of electron contamination. Monte Carlo calculations show that for the Clinac-18 10 MV photon beam, 98% of all electrons reaching the scoring plane are produced somewhere in the air between the x-ray target and the patient. The magnitude of the electron contamination rises with field size and appears to approach a saturation point at a field size that is greater than the maximum field size of 20×20 cm^2 studied in this thesis.

When the program for the simulation of the Clinac-18 treatment head was first written, programming difficulties precluded the implementation of the PRESTA electron transport algorithm. Consequently, the electron parameter data calculated for the various field sizes may come into question. Since then, the PRESTA algorithm has been implemented and further investigation into the electron contamination of the x-ray beam will be pursued in order to confirm the electron data stated in this thesis. It is the belief of the author, however, that the electron step sizes in the various media of the treatment head were chosen small enough so that the accuracy of the electron data could be assured.

The average energy of the electrons produced in the air was calculated to be approximately 2 MeV for both the flattened and the unflattened treatment beam. Application of the Klein-Nishina formula [1] to the mean photon energy of the x-ray beam predicts that for 3 MeV photons (from Figure 4.8), the mean energy of the electrons set in motion in a Compton interaction is 0.6 times the incident photon energy or 1.8 MeV. This suggests that the majority of the electrons produced in air can be attributed to Compton interactions. A 2 MeV electron has a range in water of 0.97 cm [2] and, while it is able to affect the surface dose and the build-up region very near the phantom surface, it cannot affect the position of d_{max} which for a 10 MeV x-ray beam clearly lies beyond the range of 2 MeV electrons.

3. MONTE CARLO DEPTH DOSE CALCULATIONS

The calculated photon energy spectra and the electron contamination data for the Clinac-18 operating both with (Fig. 4.1) and without (Fig. 4.4) the beam flattening filter for the various field sizes were used as the input spectra for the modified DOSRZ program supplied by EGS4. The DOSRZ program is a routine which simulates a water phantom for the calculation of percent depth doses. It samples the provided photon and electron spectral data for the various treatment fields and performs Monte Carlo calculations of the particle transport in the medium. Separate Monte Carlo percent depth dose calculations in a water phantom were performed for field sizes in the range between 2×2 cm^2 and 20×20 cm^2 for both the flattened and the unflattened x-ray beams.

The results of the PDD calculations for the various field sizes at SSD=100 cm with and without the beam flattening filter in place are plotted in Figure 4.10 (a) and (b), respectively. Several trends are manifested in the figures. As the field size is increased, the calculated surface dose also increases. This is in agreement with the predictions based on the calculated scattered photon and the electron contribution to the treatment beam as functions of the field size: as the low-energy photon contribution and the electron contamination is increased, the dose at and near the surface should increase accordingly.

The calculated PDD curves also display increased penetration into the phantom with larger field size. Observation of the tail of each curve reveals that the percent depth dose at a given depth below d_{max} is highest for the

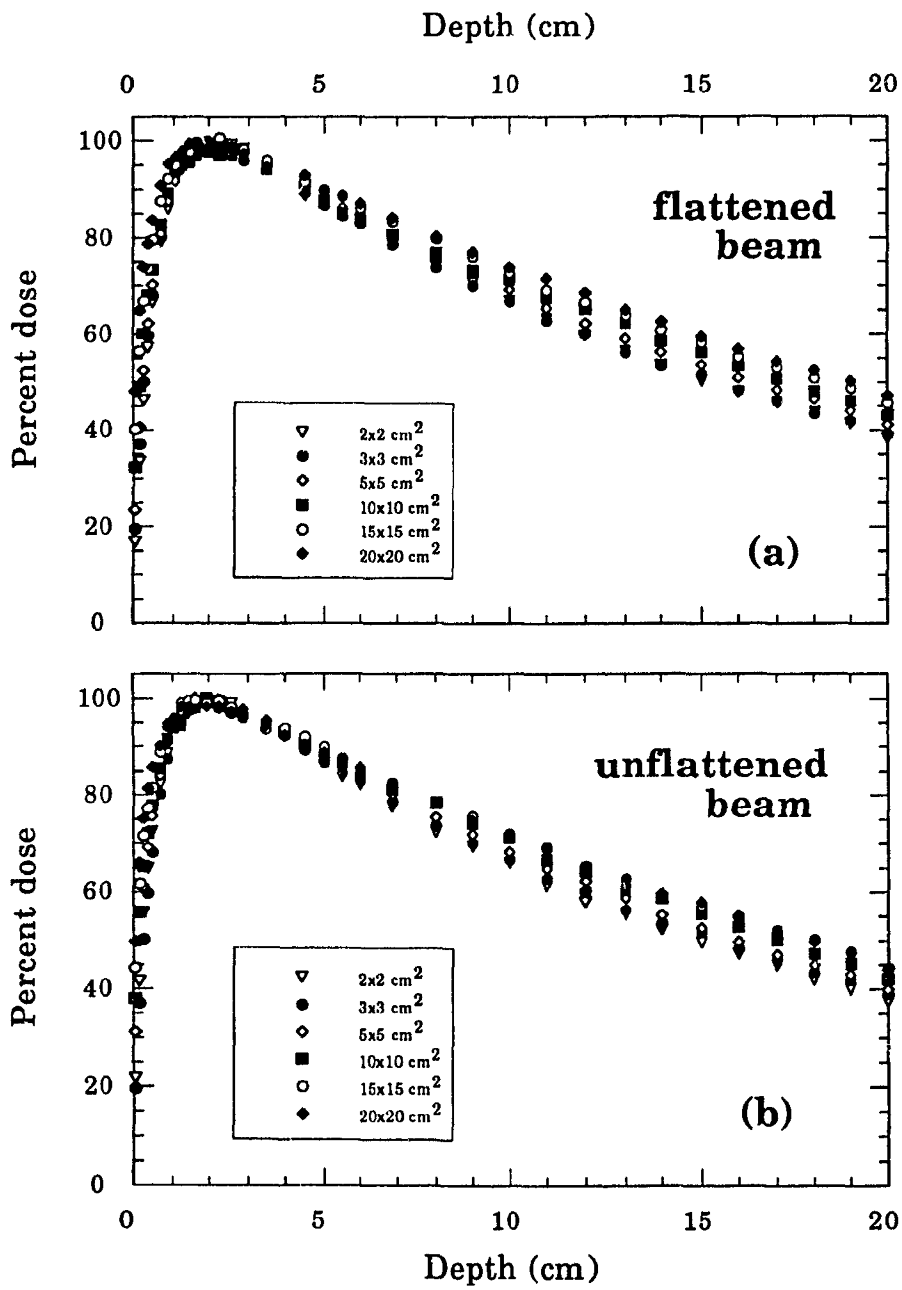

Figure 4.10 Monte Carlo calculated percent depth doses as functions of the treatment field size for the flattened (a) and the unflattened (b) Clinac-18 10 MV x-ray beam. The PDD increases with field size for both the flattened and the unflattened x-ray beams.

20×20 cm^2 field and lowest for the 2×2 cm^2 field. The percent depth dose along the central axis has been observed to increase with beam area, rapidly at first, and then much more slowly as the area is further increased [2]. This trend is observed experimentally for all photon beams since it is due the amount of scatter material in the path of the beam and not due to the beam itself [2,3]. The greater amount of phantom material for larger field sizes produces more scattered radiation at depths below d_{max}. The increase in the amount of scatter contributes to an increase in the absorbed dose below d_{max} for larger field sizes. The calculated PDDs for the flattened and unflattened x-ray beams demonstrate the initial rapid increase in PDD with field sizes up to the 10×10 cm^2 field followed by a more slowly increasing PDD as the field size is increased further. The PDDs for the 20×20 cm^2 field is only slightly larger than those for the 15×15 cm^2 field. This is expected, since above field sizes of 15×15 cm^2, the additional electrons which are produced at the field periphery in the phantom are not sufficiently energetic to reach the central axis and thus cannot contribute to the central axis percent depth dose.

For each field size, the last data point of the Monte Carlo calculated values is slightly lower than would be expected by extrapolation of the calculated curve. This is due to an oversight in the modelling of the phantom by the author. The phantom was assumed to be a 21 cm long water cylinder for all calculations. Twenty centimetres of phantom material is not sufficiently deep to provide for the backscattered radiation which is present for all measurements. The depth of the phantom material used for the Monte Carlo simulations should have included the minimum amount of excess phantom material present for each experimental measurement (preferably 10 cm). The dose fall-off region located at the exit surface of the phantom is not large enough to have an effect on the accuracy of any but the last point of each curve and therefore does not invalidate the results of the simulations.

4. DEPTH DOSE MEASUREMENTS

A series of percent depth dose measurements in water at SSD=100 cm for square fields ranging in size from 2×2 cm^2 to 20×20 cm^2 was made using the radiation field analyzer (RFA) discussed in Chapter 2. Measurements with the RFA were performed with the semiconductor detector beginning at a depth of 250 mm in the water and ending at a point somewhere above the surface of the water which is indicated by a discontinuity in the RFA-measured signal. Due to the effects of surface tension on the water surrounding the detector, the exact location of the water surface cannot be determined in this manner. Since the PDD is very sensitive to the depth in the build-up region, this method of measurement is unreliable above d_{max} (the error to the PDD due to this effect is negligible beyond d_{max}). As well, it is uncertain how the silicon detector, which has a higher atomic number than water, performs in regions of electronic imbalance. For the reasons described above, measurements made with the RFA are considered valid only at depths beyond d_{max} and have an uncertainty of less than 2% at depths greater than d_{max}. In the build-up region the PDDs were measured with an air ionization detector in a solid tissue-equivalent phantom.

The percent depth dose measurements in the build-up region were made using a Farmer end-window cylindrical parallel plate ionization chamber in combination with a polystyrene phantom. The small sensitive volume of the parallel plate detector permits accurate measurements for small radiosurgical fields as well as for larger radiotherapy fields. This configuration provides a uniquely defined surface where the origin can be assigned. Measurements made with the end-window ionization chamber were repeated once with the detector polarity at +300 V and once at -300 V. By taking the average reading of both detector polarities, the effect of Compton current on the measured data was eliminated from the final result [4]. At least three measurements at every depth for each detector polarity were taken. The uncertainty in each measurement is the sum of the standard deviations of the measurements made in both polarities at each depth.

A detailed look at the build-up region for the 3×3 cm^2 field showing the Monte Carlo-calculated PDD data as well as those measured with the RFA chambers and the parallel plate chamber is given in Figure 4.11. The calculated points closely follow the data measured with the end-window ionization chamber. In this region, while the end-window chamber data are smoothly varying, the RFA measurements become erratic as the phantom surface is approached. The error bars shown in this graph are typical of the errors in all measurements and calculations, and are not repeated in the other figures for the sake of simplicity.

By combining the data obtained using the end-window chamber in the build-up region with those obtained using the semiconductor detector at d_{max} and beyond, a complete set of PDD data as a function of field size was gathered. The RFA-measured data and the end-window chamber data were joined at the d_{max} determined by the end-window chamber measurements. This was achieved by correcting the RFA-measured values for depth by setting their d_{max} depths equal to the d_{max} found with the parallel plate ionization chamber.

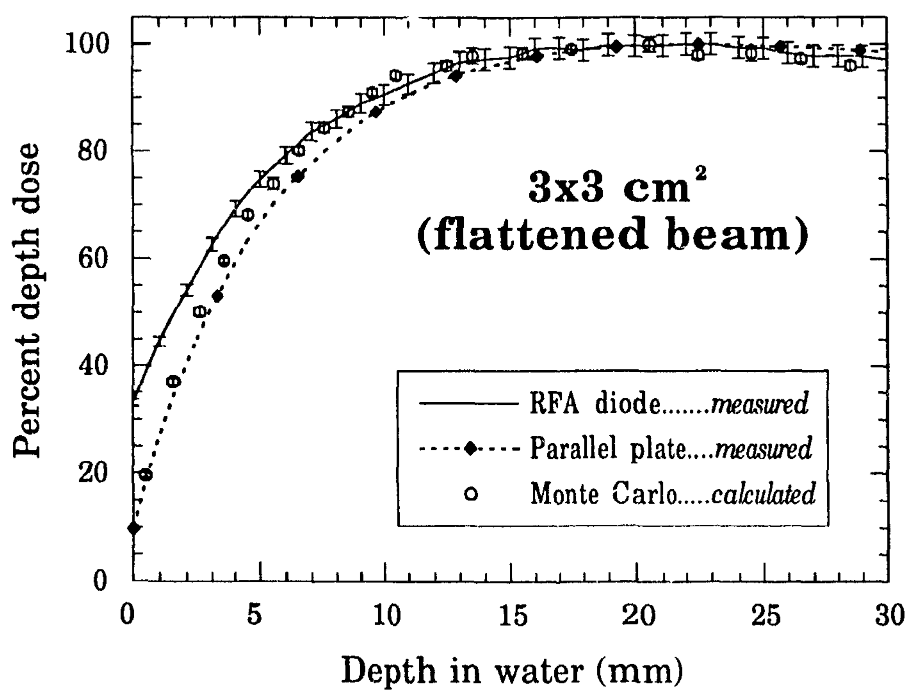

Figure 4.11 Detailed look of the build-up region for a 3x3 cm^2 field at SSD=100 cm for the flattened x-ray beam. The Monte Carlo calculated results follow the parallel plate measured data to the phantom surface.

Comparisons of the complete measured PDD and the calculated data for the flattened x-ray beams are plotted in Figure 4.12. The agreement of the calculated data with the measured ones is excellent for all field sizes despite the constraint in the physical model for the phantom. In Table 4.1 the calculated percent depth doses for the flattened beams are compared with the measured data at selected depths in the phantom. The Monte Carlo-calculated data for the unflattened x-ray beam are plotted with the measured unflattened x-ray beam data in Figure 4.13. The calculated values for the unflattened beams are compared with the measured values at various selected depths in Table 4.2. Again, the calculated values are comparable to measured data and lend credibility to the theoretical model of the Clinac-18 treatment head and the calculation method applied.

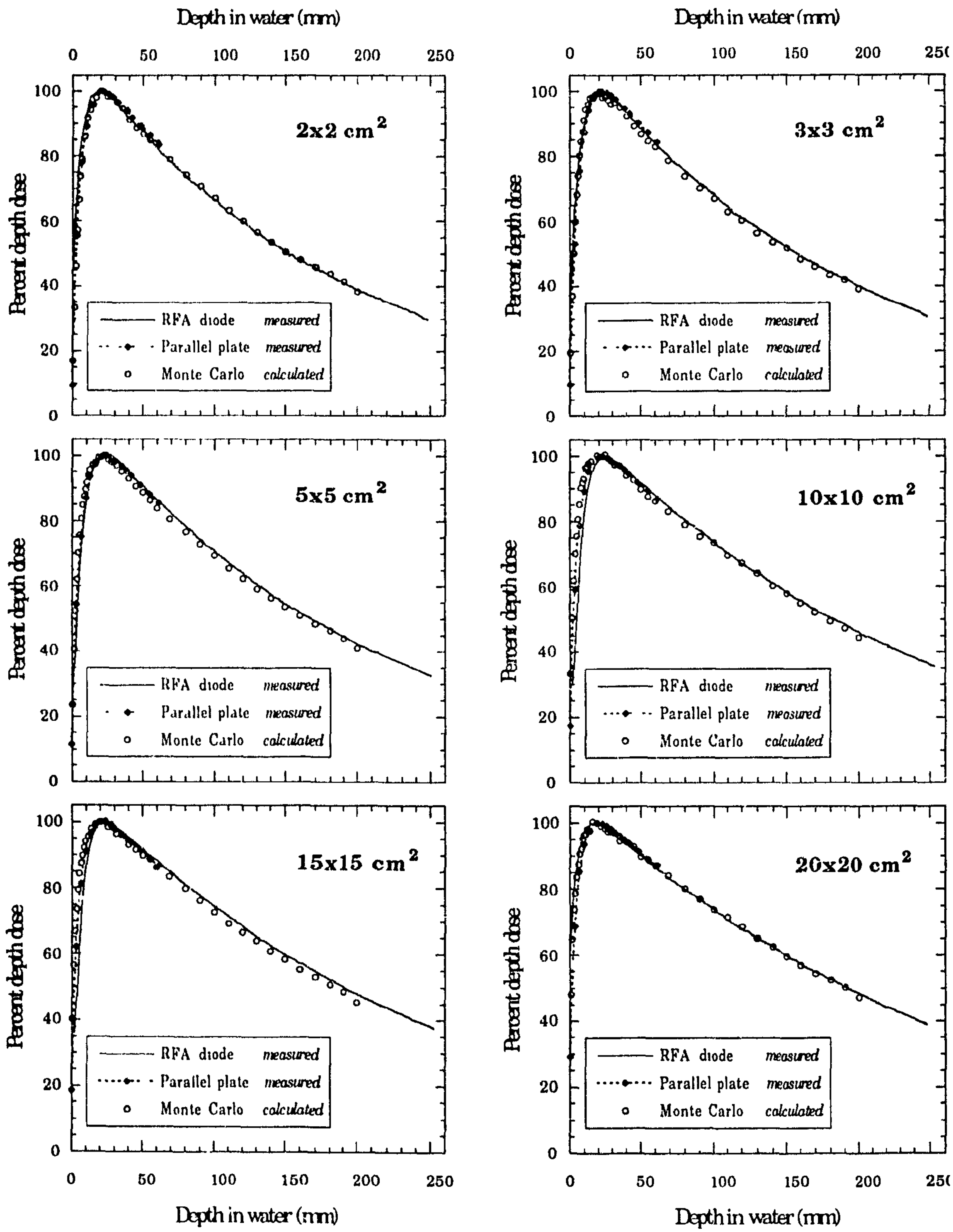

Figure 4.12 Measured and calculated percent depth doses for various field sizes for the flattened Clinac-18 10 MV x-ray beam.

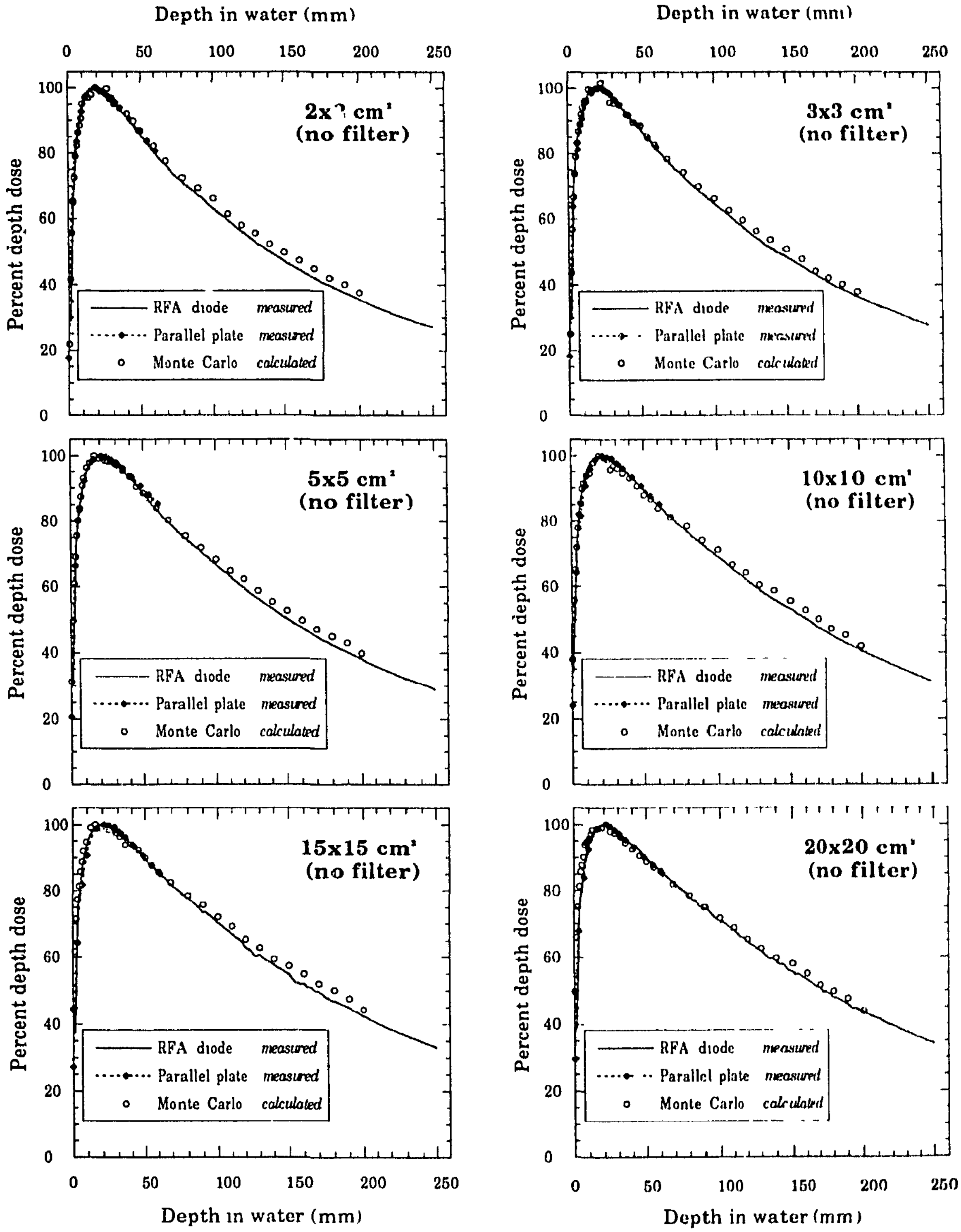

Figure 4.13 Measured and calculated percent depth doses for various field sizes for the unflattened Clinac-18 10 MV x-ray beam.

Table 4.1 Comparison of Monte Carlo calculated values (C) to measured data (M) with the beam flattening filter in place. An end-window parallel plate ionization chamber was used in the build-up region. Beyond d_{max}, the silicon diode RFA detector is used. The depth d_{max} is taken as the measured depth of maximum dose.

depth (mm)	2x2		3x3		5x5		10x10		15x15		20x20	
	C	M	C	M	C	M	C	M	C	M	C	M
5	70.2	68.0	71.1	65.4	72.9	65.9	78.0	69.9	78.0	72.7	85.5	77.9
dmax	99.2	100	98.5	100	100.4	100	100	100	99.8	100	99.3	100
50	86.8	87.5	86.8	86.6	88.6	90.8	89.9	91.6	89.8	91.9	89.9	90.1
100	67.0	66.3	66.8	68.5	69.3	70.7	73.5	73.6	72.7	74.1	73.9	73.6
150	50.5	50.7	51.8	52.0	53.7	54.7	58.0	58.7	58.4	59.9	59.6	59.8
200	38.3	38.7	39.1	40.0	41.0	42.2	44.4	46.3	45.6	48.0	47.2	48.3

Table 4.2 Comparison of Monte Carlo calculated values (C) to measured data (M) without the beam flattening filter. An end-window parallel plate ionization chamber was used in the build-up region. Beyond d_{max}, the silicon diode RFA detector is used. The depth d_{max} is taken as the measured depth of maximum dose.

depth (mm)	2x2		3x3		5x5		10x10		15x15		20x20	
	C	M	C	M	C	M	C	M	C	M	C	M
5	75.8	75.5	76.5	73.4	77.9	75.7	79.9	74.0	83.6	74.0	86.7	77.9
dmax	100	100	100.2	100	99.5	100	99.5	100	99.6	100	99.7	100
50	86.9	85.4	88.7	86.6	88.5	88.4	87.9	89.6	89.9	89.9	88.8	90.1
100	66.1	63.2	66.3	64.8	68.4	66.8	71.3	69.1	72.0	70.3	71.6	70.5
150	49.7	47.2	50.8	48.5	52.6	50.1	55.7	53.0	57.4	54.9	57.9	55.4
200	37.6	35.6	38.0	36.4	39.9	38.1	42.1	40.4	44.3	42.5	44.0	41.7

5. MEASUREMENTS IN THE BUILD-UP REGION

Special attention is paid to the measurement of the dose in the build-up region because it is in this region that the percent depth dose is the most sensitive to small changes in the radiation source. Small amounts of electron contamination as well as low-energy scattered photons can have large effects on the surface dose delivered to the patient. These low-energy photons which are produced in the linac treatment head are sufficiently numerous to affect the position of d_{max} in the patient and merit further study.

5.1. The surface dose

An investigation of the doses delivered to the surface of the phantom as a function of the field size reveals that, as the field size is increased, the surface dose also increases. This increase in the surface dose with an increasing field size is due to a combination of two factors: (1) backscattered photons from the phantom material and (2) electrons produced in air which deposit their energy directly at the phantom surface. High-energy photons interact with the medium to produce high-energy electrons which, in order to conserve momentum, travel primarily in the forward direction slowly losing their energy in secondary collisions. Since the electron range in a medium is an increasing function of the kinetic energy, higher energy electrons deposit their energy at greater depths in the phantom. Thus, a high-energy photon beam produces a lower surface dose than a low-energy beam [2,3,4]. Since the flattened 10 MV x-ray beam is more energetic than the unflattened beam, it is expected that the surface dose for the flattened beam will be lower than that for the unflattened beam. The measured surface doses for the flattened and unflattened x-ray beams as functions of the field size are shown in Figure 4.14 where, as expected, the surface dose for the flattened beam is lower than for the unflattened beam for all field sizes. However, the rates of change of the surface doses with field size produced by the flattened and unflattened x-ray beams are different.

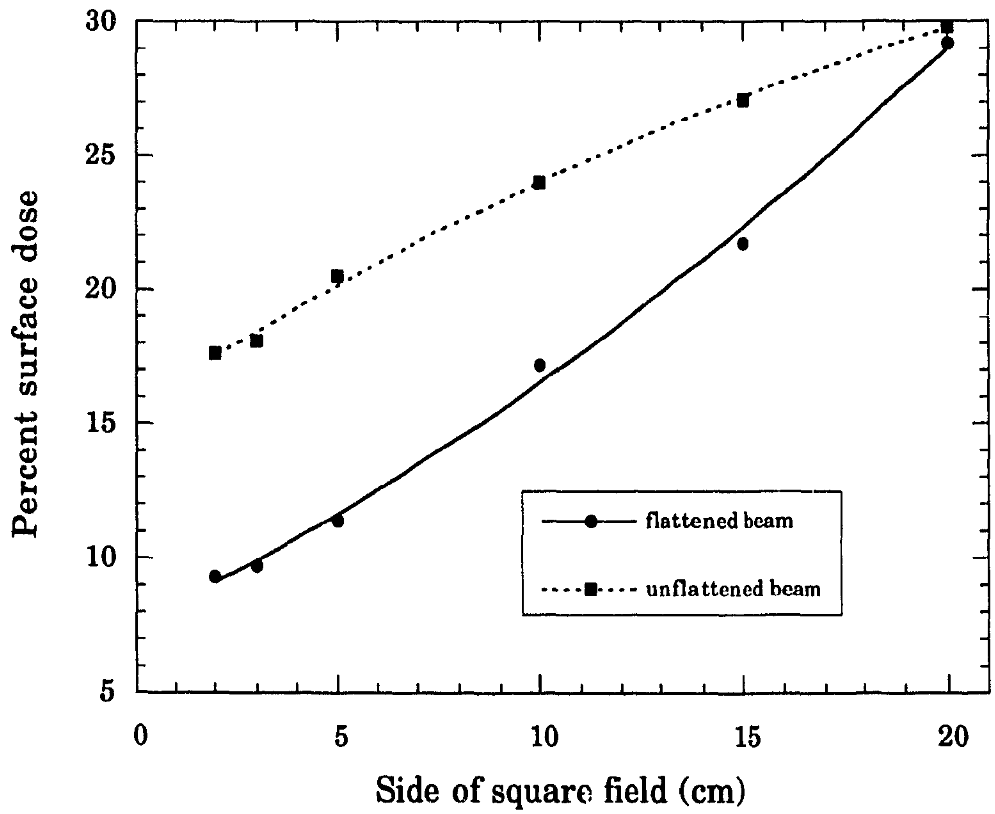

Figure 4.14 Measured surface dose as a function of the field size for the flattened and unflattened x-ray beams. Surface doses have been normalized to the dose at d_{max} for each field size. The surface dose for the flattened x-ray beam is lower than for the unflattened beam, however, it increases at a greater rate with increasing field size.

The slope of the surface dose with field size for the flattened beam is greater than that for the unflattened beam. Observation of the calculated percent electron contamination for the flattened and unflattened x-ray beams (Figure 4.9) reveals that neither the differences in the surface dose nor the differences in the slopes of the surface dose as a function of the field size for the flattened and unflattened beams is due to the electron contamination since the electron contamination is roughly equal for flattened and unflattened beams. The only remaining possibility is that the photon spectrum is responsible for the difference in surface dose for the flattened and unflattened beams as well as the difference in the rate of change of the surface dose as a function of the field size. The higher surface dose delivered by the unflattened x-ray beam is consistent with the fact that the average calculated photon energy of the flattened x-ray beam is significantly higher than that of the unflattened x-ray beam. As well, the average photon energy of the total *flattened* photon beam decreases at a much faster rate with increased field size than that of the *unflattened* beam. This is reflected in the greater change of the surface dose for the flattened x-ray beam with increased field size over the unflattened beam.

5.2. The shift in d_{max}

For each field size, the depths of maximum dose were found by fitting an interpolation function to the dose measurements made with the end-window ionization chambers and estimating the maximum of the curve. The estimation of d_{max} was repeated 6 times and the mean of the 6 estimations was taken

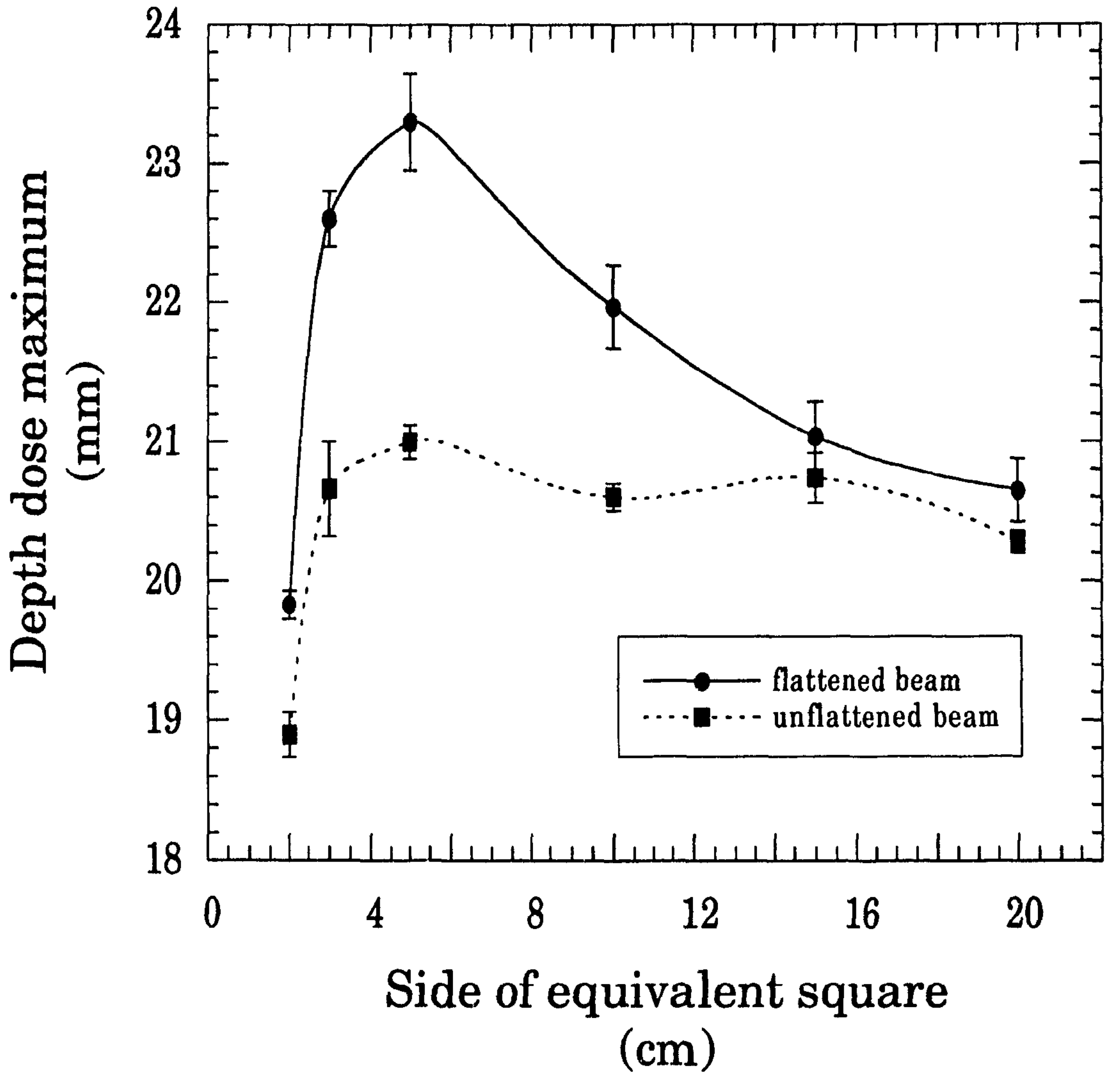

Figure 4.15 Graph showing d_{max} in polystyrene as a function of the field size for the Clinac-18 linear accelerator for the flattened and unflattened x-ray treatment beams. With the flattening filter in place, the depth of d_{max} is maximum for a 5×5 cm^2. Without the flattening filter, d_{max} reaches a nearly constant value for fields larger than 5×5 cm^2.

as the true d_{max}. The depths of d_{max} in the polystyrene phantom produced by the Clinac-18 10 MV x-ray beam both with and without the photon beam flattening filter in place are shown in Figure 4.15 and tabulated in Table 4.3. For the flattened photon beam, d_{max} first increases with field size at small fields then reaches a maximum depth of 23.3 ± 0.4 mm for fields around 5×5 cm^2, and then steadily decreases as the field size is further increased to large values. When the beam flattening filter is rotated out of the path of the x-ray beam and the beam remains unfiltered, d_{max} increases with field size for radiosurgical fields, reaches a maximum depth of 21 mm for the 5×5 cm^2 field but remains roughly constant as the field size is increased above 5×5 cm^2. These observations are in agreement with results reported by Sixel and Podgorsak [5] and Sixel [6] who also found that with the beam flattening filter in place, d_{max}

Table 4.3 Depth of maximum dose for the Clinac-18 with and without the flattening filter for various field sizes measured using a Farmer end-window parallel plate ionization chamber.

Field Size (cm x cm)	2x2	3x3	5x5	10x10	15x15	20x20
depth (filter) (mm)	19.8	22.6	23.3	22.0	21.0	20.7
depth (no filter) (mm)	18.9	20.7	21.0	20.6	20.7	20.3

reaches a maximum value for a field size of 5×5 cm^2. For unflattened beams, Sixel reported a d_{max} increases with field size for small fields and a saturation d_{max} value for all fields above 4×4 cm^2. Similar results were reported previously for x-ray beams of different energy by Arcovito *et al* [7].

In Chapter 2, a description of the dose deposition process was given which predicted that the depth of maximum dose should increase with an increasing field size until reaching a saturation point after which d_{max} should remain constant and independent of the field size provided that the spectrum of incident particles is constant. The fact that the d_{max} for the flattened 10 MV x-ray beam reaches a maximum value and then decreases with increasing field size is inconsistent with the hypothesis that the x-ray spectrum of the Clinac-18 is independent of field size. When the flattening filter is removed from the path of the treatment beam, however, d_{max} changes according to the constant-beam hypothesis. The shift in d_{max} with field size was predicted by the Monte Carlo calculations and verified experimentally. Given that the only difference between the flattened and the unflattened x-ray beams is the presence of the photon flattening filter, a conclusion may be reached that any field size dependence of the flattened x-ray beam must be caused by scatter from the flattening filter. This is consistent with the Monte Carlo calculated x-ray spectra where it was shown that the flattening filter was responsible for nearly all of the low-energy scattered photons produced in the Clinac-18 treatment head.

6. REFERENCES

1. W. Heitler: The quantum theory of radiation. Oxford University Press, New York (1954).

2. H.E. Johns, J.R. Cunningham: The Physics of Radiology, 4th edition. Charles C. Thomas, Springfield, Illinois (1983).

3. F.M. Khan: The Physics of Radiation Therapy, 2nd edition. Williams and Wilkins, Baltimore, Maryland (1992).

4. H.E. Attix: Introduction to Radiological Physics and Radiation Dosimetry. John Wiley and Sons, Toronto, Ontario (1986).

5. K.E. Sixel: Measurement and Monte Carlo Simulations of X-ray Beams in Radiosurgery. Thesis paper, Faculty of Graduate Studies and Research, McGill University (1993).

6. K.E. Sixel, E.B. Podgorsak: *Buildup region and depth of dose maximum of megavoltage x-ray beams*, Med. Phys. **21**, 411 (1994).

7. G. Arcovito, A. Piermattei, G. D'Abramo, and R.A. Bassi: *Dose measurements and calculations of small radiation fields for 9 MV x rays.* Med. Phys. **20**, 779 (1985).

CHAPTER 5
CONCLUSIONS

1. SUMMARY

Measurements of the central-axis percent depth dose (PDD) in tissue-equivalent phantoms for the flattened and unflattened clinical 10 MV x-ray beam produced by the Clinac-18 linear accelerator were conducted for various field sizes ranging from small radiosurgical fields to relatively large fields used in standard radiotherapy. A two-step Monte Carlo calculation of the percent depth dose deposition of the Clinac-18 10 MV x-ray beam for the various treatment field sizes produced results which were in excellent agreement with measured data. Given that the PDD calculations are the result of the second stage of the simulation process and that they were based on the spectral information calculated in the first stage of the simulation, the agreement between the calculated and the measured PDDs implies: (i) the correctness of the calculated spectral data, (ii) the usefulness of the EGS4 program in clinical dosimetry, and (iii) the adequacy of our particular model of the linac treatment head.

2. SPECTRAL CALCULATIONS

The Monte Carlo simulation of the Clinac-18 treatment head is an excellent means of characterizing the 10 MV x-ray treatment beam used in radiotherapy. The Monte Carlo method for determining the x-ray beam characteristics is probably the most reliable and accurate method available for extremely high-output modern linear accelerators. The Monte Carlo simulations allow for the calculation of the particle spatial distributions and the complete photon-energy spectra for any configuration of the treatment head.

2.1. Photon energy spectra

The calculations of the flattened x-ray beam photon-energy spectra for field sizes ranging from 2×2 cm^2 to 20×20 cm^2 revealed that for small fields the treatment beam consists of only a very small amount of scattered radiation (1.5%), but as the field size is increased, the contribution of scattered radiation to the x-ray beam reaching the patient also increases amounting to 11.5% for the 20×20 cm^2 field. An analysis of the influence of each of the treatment head components on the total treatment beam revealed that the flattening filter, which is used to improve the beam characteristics by producing an uniform dose deposition at a depth of 10 cm in the phantom, produces most of the scattered photon contamination. The scattered photons created in the flattening filter eventually lead to an undesirable increase in the surface dose to the patient, and attempts should be made to eliminate them from the treatment beam.

The primary-photon component of the flattened beam remains relatively unchanged as the field size is increased, however, the shape of the primary-photon spectra is a function of the field size. It was found that the contribution of high-energy photons to the primary beam decreases slightly with increasing field size due to the conical shape of the flattening filter. Since the flattening filter is thinner at its periphery, it attenuates the portions of the x-ray beam that are further away from the axis less than it attenuates the beam passing through the central axis, therefore the x-ray mean energy of the total primary beam decreases with increasing field size.

When the flattening filter was omitted from the calculations, the scatter profile of the x-ray beam was improved remarkably: the amount of scatter in the unflattened treatment beam decreased to 0.6% from 1.5% for the flattened beam for a 2×2 cm^2 field. The contribution of scatter to the unflattened x-ray beam also increased as the field size was increased, yet even at fields as large as 20×20 cm^2, the calculated amount of scatter reached only 3.5% of the total treatment beam and was comparable to that for the smallest flattened beam. The unflattened primary photon-energy spectra did not change with field size; however, the removal of the flattening filter increased the quantity of low-energy photons comprising the primary beam. The unflattened primary photon beam is much less energetic than the flattened primary beam and therefore is a less penetrating beam. The lower energy photon beam produced without the flattening filter delivered a higher surface dose than the flattened treatment beam.

2.2. Electron contamination

The Monte Carlo calculations showed that the electron contamination of the 10 MV x-ray beam was due primarily to electrons produced in the air between the x-ray source and the patient. Both the flattened and the unflattened treatment beams produced similar amounts of electron contamination, therefore, one can conclude that the flattening filter is not a factor in the production of electrons. Calculation of the mean electron energy revealed that most of the electrons reaching the patient are not sufficiently energetic to reach the depth of maximum dose and, therefore, cannot affect the position of d_{max} in the phantom, however, these electrons may still contribute significantly to the surface dose.

3. THE SURFACE DOSE

Measurements of the percent depth dose in the build-up region confirmed that the surface dose increases as the field size is increased. For the flattened x-ray beam, the surface dose varies between 9% of the d_{max} value for the 2×2 cm^2 to 29% for the 20×20 cm^2 field. For the unflattened x-ray beam, the surface dose ranges from 17% to 30% for the 2×2 cm^2 and the 20×20 cm^2 fields, respectively. The surface dose of the unflattened treatment beam is higher than that of the flattened beam because the mean energy of the photons comprising the primary beam is much lower than the mean energy of the flattened primary beam.

Since the calculated primary photon-energy spectra for the flattened and the unflattened treatment beams were found to be independent of the field size, any change in the surface dose with changing field size must have been due to scatter contamination. The contaminating electrons contribute to the surface dose and most likely are the cause of the increase in surface dose with field size for the unflattened beam since the scattered photon contribution for this beam is quite low. Given that the calculated electron contamination of the flattened and unflattened x-ray beams is approximately equal for each field size, the higher rate of increase in the surface dose with increasing field size must be attributed to low-energy scattered photons. The low-energy scattered photons produced in the x-ray flattening filter contribute a significant amount to the surface dose and to the dose in the build-up region.

4. THE SHIFT IN d_{max}

For all field sizes, the depth of maximum dose for the flattened x-ray beam was greater than that for the unflattened beam owing to the improved penetrability of the flattened beam. The measured d_{max} in the solid phantom for the flattened x-ray beam increases with increasing field size for field sizes between 2×2 cm^2 and 5×5 cm^2. Around 5×5 cm^2 d_{max} reaches a saturation value; d_{max} ranges from 19.8 mm for the 2×2 cm^2 field to 23.3 mm for the 5×5 cm^2 field. As the field size is increased beyond 5×5 cm^2, d_{max} decreases steadily to a nearly asymptotic value of 20.7 mm for the 20×20 cm^2 field. For the unflattened x-ray beam d_{max} is at 18.9 mm depth for the 2×2 cm^2 field, reaches a maximum value of 20.6 mm for a field of 5×5 cm^2 and then remains approximately constant as the field size increases further.

The scattered photon contamination produced in the flattening filter is the only possible explanation for the decrease in d_{max} as the field size is increased beyond 5×5 cm^2 for the flattened beam, as the majority of the contaminating electrons are insufficiently energetic to penetrate as deep as d_{max}. There is only a minute observed shift in d_{max} for the unflattened x-ray beam for fields larger than 5×5 cm^2 because the amount of scatter in the unflattened beam is negligible, whereas the flattened beam becomes degraded so severely for larger fields that the dose in the build-up region, including d_{max} and the dose at the phantom surface, approaches that of the unflattened beam. Clearly, this is an undesirable effect and must be considered when designing a linac for radiation therapy.

5. FUTURE WORK

This thesis represents a Monte Carlo and experimental study of clinical x-ray beams produced by a 10 MV Clinac-18 linear accelerator. The effects on the x-ray beam of the various components comprising the linac head are investigated and some shortcomings of the existing design are identified. Additional work could concentrate on ways to improve the usefulness of the current clinical 10 MV beam. An investigation of different target and flattening filter materials and thicknesses should be made in order to optimize the primary component of the x-ray beam. As well, the study should include an investigation of the scattered photon spectra produced by the different flattening filter materials in the hopes of minimizing the scatter induced degradation of the treatment beam.

A worthy area for study would be into the redesigning of the linac to eliminate the need for a flattening filter altogether. By constantly moving the position where the electrons bombard the x-ray target, an x-ray beam of even intensity and uniform characteristics could be produced. This type of linac would have to employ electron energies in excess of 10 MeV since the surface dose and the depth of d_{max} for the unflattened beam are not satisfactory.

It would also seem practical to attempt to extend the evacuated region to include the entire linac treatment head up to the location of the ionization chamber. Such a design would reduce the electron contamination produced in air and improve the skin dose delivered to the patient. This redesign of the modern medical linac would lead to an improved skin dose, a greater depth of maximum dose, and increased penetrability of the treatment beam into the patient, all of which would improve the treatment technique for the patient as well as the probability for curing the disease.

BIBLIOGRAPY

1. Aldrich, J., J. Andrew, H. Michaels, P. O'Brien: Characteristics of the photon beam from a new 25-MV linear accelerator, Med. Phys. **12**, 619 (1985). (5)

2. American Association of Physicists in Medicine, RTC Task Group 21: *A protocol for the determination of absorbed dose from high energy photon and electron beams,* Med. Phys. **10**, 741 (1983). (36)

3. Arcovito, G., A. Piermattei, G. D'Abramo, and R.A. Bassi: *Dose measurements and calculations of small radiation fields for 9 MV x rays.* Med. Phys. **20**, 779 (1985). (99)

4. Attix, H.E. : Introduction to Radiological Physics and Radiation Dosimetry. John Wiley and Sons, Toronto, Ontario (1986). (88,94)

5. Berger, M.J., S.M. Seltzer: *ETRAN, Monte Carlo code system for electron and photon transport through extended media,* Documentation for RSIC computer dose package CCC-107, Oak Ridge National Laboratory, Oak Ridge, Tennessee (1973). (47)

6. Berger, M.J., S.M. Seltzer: *Stopping powers and ranges of electrons and positrons,* NBS report NBSIR 82-2550-A (1983). (48)

7. Bielajew, A.F., D.W.O. Roges: PRESTA: *The parameter reduced electron-step transport algorithm for electron Monte Carlo transport*, Nuc. Instr. Meth. Phys. Res. **B18**, 165 (1987). (56)

8. Bielajew, A.F., D.W.O. Rogers: *Variance reduction techniques, in:* Monte Carlo transport of electrons and photons, T.M. Jenkins, W.R. Nelson, A. Rindi (eds.), Plenum Publishing Co., New York, (1987), pp.407-419. (55)

9. Biggs, P. J., C. C. Ling: *Electrons as the cause of the observed* d_{max} *shift with field size in high energy photon beams*, Med. Phys. **6**, 291, (1979). (5)

10. Biggs, P.J., M.D. Russell: *An investigation into the presence of secondary electrons in megavoltage photon beams*, Phys. Med. Biol. **9**, 1033 (1983). (5)

11. Brown, K.L., W.G. Turnbull: *Achromatic magnetic beam deflection system,* U.S. Patent 3 876 635, issued 1975. (31)

12. Bureau of Radiological Health and the Training Institute Environmental Control Administration: Radiological Health Handbook. U.S. Department of Health, Education, and Welfare (1970). (12)

13. Clinac-18 maintenance manual, volume 1, Varian Associates, Palo Alto, California (1975). (22,26,29,32,33,34,35)

14. Cook, A. J., L. J. Shustek: *EGS4 User guide to Mortran3*, SLAC report 265, Stanford Linear Accelerator center, Stanford, California (1985). (47)

15. Coutard, H. : *Roentgentherapy of epitheliomas of the tonsillar region, hypopharynx and larynx from 1920 to 1926.* Am. J. Roentgenol. **28**, 313, (1932). (3)

16. Ford, R. L., W. R. Nelson: *The EGS code system (Version 3),* SLAC report 210, Stanford Linear Accelerator center, Stanford, California (1978). (47)

17. Heitler, W.: The quantum theory of radiation. Oxford University Press, New York (1954). (83)

18. ICRU report # 37, *Stopping powers for electrons and positrons*, International Commision on Radiation Units and Measurements, Washington, DC (1984). (48)

19. Johns, H. E., J. R. Cunningham: The Physics of Radiology, 4th edition. Charles C. Thomas, Springfield, Illinois, U.S.A. (1983). (10,12,28,83,86,94)

20. Johns, H.E., E.R. Epp, D.V. Cormak, S.O. Fedoruk: *Depth dose data and diaphragm design for the Saskatchewan 1,000 curie cobalt unit*, Brit. J. Radiol. **25**, 302 (1952). (4)

21. Karzmark, C.J., R.J. Morton: A primer on theory and operation of linear accelerators in radiation therapy, U.S. Department of Health and Human Services, Food and Drug Administration, Bureau of Radiological Health, Maryland (1981). (25)

22. Karzmark, C.J., C.S. Nunan, E. Tanabe: Medical Electron Accelerators, McGraw-Hill, Inc (1983). (28,31)

23. Khan, F.M.: The Physics of Radiation Therapy, 2nd edition. Williams & Wilkins, Maryland, U.S.A. (1994). (12,16,39,83,94)

24. Klevenhagen, S.C.: Physics of Electron Beam Therapy, Medical Physics Handbook 13, Adam Hilger Ltd, England (1985). (26,27)

25. Knapp, E.A., B.C. Knapp, J.M. Potter: *Standing wave high energy linear accelerator structures*, Rev. Sci. Instr. **39**, 979 (1968). (29)

26. Leung, P.M.K., M.R. Sontag, H. Maharaj, S. Chenery: *Dose measurements in the build-up region for Cobalt-60 therapy units*, Med. Phys. **3**, 169 (1976). (4)

27. Luxton, G., M.A. Astrahan: *Characteristics of the high-energy photon beam of a 25-MeV accelerator*, Med. Phys. **15**, 82 (1988). (5)

28. Marbach, J.R., P. Almond: *Scattered photons as the cause for the observed d_{max} shift with field size in high-energy photon beams*, Med. Phys. **4**, 310 (1977). (5)

29. Mayneord, W.V.: *The significance of the Röntgen,* Acta Int. Union Against Cancer **2**, 271 (1937). (37)

30. Mohan, R., C. Chui: *Energy and angular distributions of photons from medical linear accelerators*, Med. Phys. **12**, 592 (1985). (6)

31. Moss, W. T., W. M. Brand, H. Battifora: Radiation Oncology, Rationale, Technique, Results, 5th edition, C. V. Mosby Company, Missouri (1979). (2)

32. Nelson, W.R., H. Hirayama, D.W.O. Rogers: *The EGS4 code system*, SLAC report 265, Stanford Linear Accelerator center, Stanford, California (1985). (47,48)

33. Nelson, W.R., H. Hirayama, D.W.O. Rogers: *EGS4 flow diagrams*, SLAC report 265, Stanford Linear Accelerator center, Stanford, California (1985). (51)

34. Orton, C.G., J.B. Seibert: *Surface effects of high-energy x rays at oblique incidence*, Brit. J. Radiol. **44**, 895 (1971). (4)

35. Padikal, T.N., J.A. Dey: *Electron contamination of a high-energy x-ray beam*, Phys. Med. Biol. **23**, 1086 (1978). (5)

36. Perez, C.A., L.W. Brady: <u>Principles and Practice of Radiation Oncology,</u> J.B. Lippincott Company, Philadelphia, Pennsylvania (1987). (3)

37. Rao, P.S., K. Pillai, E.G. Gregg: *Effect of shadow trays on surface dose and build-up for megavoltage radiation*, Am. J. Roentgenol. **117**, 168, (1973). (4)

38. Rawlinson, J.A.: *High energy x -ray beams in radiotherapy*, Med. Phys. **1**, 95 (1974) (abstract). (5)

39. Rikner, G.: *Characteristics of a selectively shielded p-si detector in* ^{60}Co *and 8 and 16 MV Roentgen radiation,* Acta. Radiol. Oncol. **24**, 205 (1985). (38)

40. Rikner, G., E. Grussel: *Selective shielding of a p-si detector for quality independence*. Acta. Radiol. Oncol. **24**, 65 (1985). (38)

41. Roentgen, W.C.: *On a new kind of rays* (preliminary communication). Translation of a paper read before the Physikalischemedizinische Gesellschaft of Wurzburg on 28 December, 1895. Brit. J. Radiol. **4**, 32, (1931). (1)

42. Rogers, D.W.O., A.F. Bielajew: *Monte Carlo techniques of electron and photon transport for radiation dosimetry*, in: The dosimetry of ionizing radiation, vol. 3, K.R. Kase, B.E. Bjärngard, F.H. Attix (eds.). Academic Press, San Diego, California (1990), pp.427-540. (44)

43. Scanditronix customer documentation: *The energy compensated (filtered) GR-p EC detector for water phantom measurements in photon fields*. Frank Barker Associates Inc., New Jersey. (38)

44. Segrè, E.: Nuclei and Particles, W. A. Benjamin, Inc., New York (1965). (9)

45. Sixel, K.E.: Measurement and Monte Carlo Simulations of X-ray Beams in Radiosurgery. Thesis paper, Faculty of Graduate Studies and Research, McGill University (1993). (98)

46. Sixel, K.E., E.B. Podgorsak: *Buildup region and depth of dose maximum of megavoltage x-ray beams*, Med. Phys. **21**, 411 (1994). (6,98)

47. Varian, R.H., S.F. Varian: *A high frequency oscillator and amplifier*, Journal of Applied Physics **10**, 321 (1939). (26)

48. Yaffe, M., K.W. Taylor, H.E. Johns: *Spectroscopy of diagnostic x-rays by a Compton-scatter method*, Med. Phys. **3**, 328, (1976). (9)